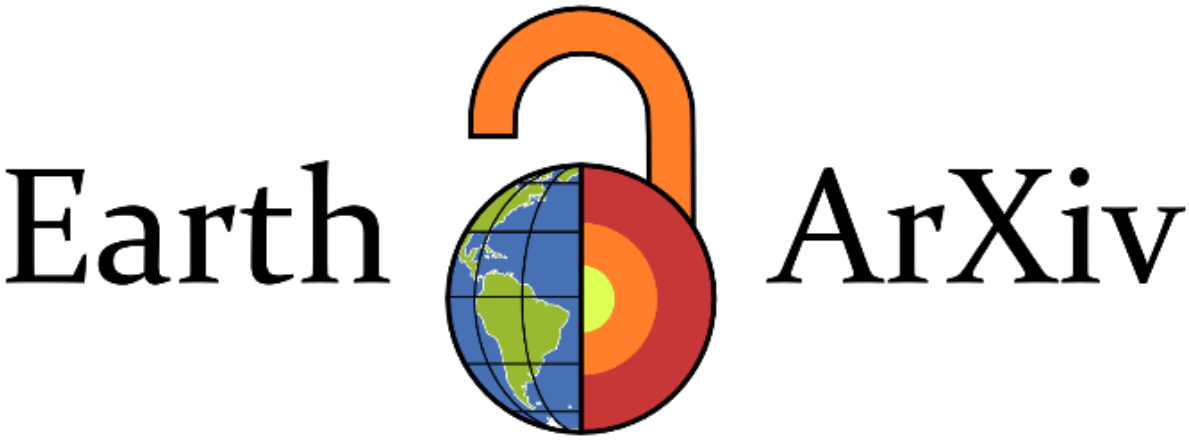

Influence and Prediction of Planetary Orbital Changes on Earth's Atmospheric Water Vapor Variations

Longhao Xu[1†], Kebiao Mao[2*, †], Sayed M. Bateni[3,4], Mengmeng Cao[2], Timothy Dube[5], Zhonghua Guo[1], Babatunde Abiodun[6], Zijin Yuan[2], Malik Maaza[4]

[1]School of Civil and Hydraulic Engineering/ School of Physics and Electronic-Engineering, Ningxia University, Yinchuan, 750021, China.
[2]State Key Laboratory of Efficient Utilization of Arid and Semi-arid Arable Land in Northern China, Institute of Agricultural Resources and Regional Planning, Chinese Academy of Agricultural Sciences, Beijing, 100081, China.
[3]Department of Civil and Environmental Engineering and Water Resources Research Center, University of Hawaii at Manoa, Honolulu, HI 96822, USA.
[4]UNESCO-UNISA Africa Chair in Nanoscience and Nanotechnology College of Graduates Studies, University of South Africa, Muckleneuk Ridge, Pretoria, 392, South Africa.
[5] Department of Earth Sciences, The University of the Western Cape, Bellville 7535, South Africa.
[6]Department of Environmental and Geographical Science, University of Cape Town, Cape Town, 7700, South Africa.

*Correspondence to: maokebiao@caas.cn; Tel.: +86-010-8210-8769

†These authors contributed equally to this work and should be considered co-first authors.

Declarations:

Conflict of Interest: The authors declared that they have no conflict of interest.

Funding: Key Project of Natural Science Foundation of Ningxia Department of Science and Technology (No. 2024AC02032), Fengyun Satellite Application Pilot Program "Development and Application of Fengyun all-weather Land Surface Temperature Spatiotemporal Fusion Dataset" (FY-APP-2022.0205).

Acknowledgments: The authors thank the U.S. Department of Energy's Office of Science Biological and Environmental Research (BER), the National Oceanic and Atmospheric Administration (NOAA) Office of Climate Programs, the NOAA Physical Sciences Laboratory, and the European Centre for Medium-Range Weather Forecasts (ECMWF) for providing climate reanalysis data, the Scripps Institution of Oceanography for providing carbon dioxide concentrations, and the NASA Jet Propulsion Laboratory Development Ephemeris for the solar system ephemeris, and the International Earth Rotation and Reference Systems Service Rapid Service/Prediction Centre for daylength data.

Citation: Xu L., Mao K., Sayed M., Cao M, Dube T., Guo Z., Abiodun B., Yuan Z., Maaza M., Influence and Prediction of Planetary Orbital Changes on Earth's Atmospheric Water Vapor Variations, EarthArXiv, 2025, 1, DOI:***.

Subjects

Education, Engineering, Physical Sciences and Mathematics

Keywords

Planetary Orbital Variations, Earth’s Water Vapor Changes, Climate Change

Influence and Prediction of Planetary Orbital Changes on Earth's Atmospheric Water Vapor Variations

Longhao Xu[1†], Kebiao Mao[2*, †], Sayed M. Bateni[3,4], Mengmeng Cao[2], Timothy Dube[5], Zhonghua Guo[1], Babatunde Abiodun[6], Zijin Yuan[2], Malik Maaza[4]

[1]School of Civil and Hydraulic Engineering/ School of Physics and Electronic-Engineering, Ningxia University, Yinchuan, 750021, China.

[2]State Key Laboratory of Efficient Utilization of Arid and Semi-arid Arable Land in Northern China, Institute of Agricultural Resources and Regional Planning, Chinese Academy of Agricultural Sciences, Beijing, 100081, China.

[3]Department of Civil and Environmental Engineering and Water Resources Research Center, University of Hawaii at Manoa, Honolulu, HI 96822, USA.

[4]UNESCO-UNISA Africa Chair in Nanoscience and Nanotechnology College of Graduates Studies, University of South Africa, Muckleneuk Ridge, Pretoria, 392, South Africa.

[5] Department of Earth Sciences, The University of the Western Cape, Bellville 7535, South Africa.

[6]Department of Environmental and Geographical Science, University of Cape Town, Cape Town, 7700, South Africa.

*Correspondence to: maokebiao@caas.cn; Tel.: +86-010-8210-8769

†These authors contributed equally to this work and should be considered co-first authors.

Abstract: A few people have gradually realized that the superposition effect of different planets in the solar system on Earth under high-speed motion and dynamic equilibrium can sometimes trigger extreme natural disasters. Due to the relatively regular changes in the relative positions of the Sun, Moon, and Earth, this study considers these three planets as independent systems. The orbits of other planets in the solar system have relatively complex changes in their positions relative to Earth, so they are considered as a whole. By constructing a dynamic quantification model based on proximity difference to eliminate the interference of internal variability of the Earth and extract the influence of different planetary orbit changes on the variation of atmospheric water vapor content, the analysis shows that Earth's rotation accounts for 4%, the Moon's revolution 10%, Earth's revolution 71%, and other planetary orbits 15% of the total impact of planetary orbital changes on atmospheric water vapor. Finally, an LSTM deep learning model was constructed to predict the changes in atmospheric water vapor content on Earth over the next decade, and the results showed that atmospheric water vapor will show a slow upward trend in the future. The research results not only provide a new perspective for understanding the mechanisms of climate change on Earth, but also provide valuable references for the study of climate evolution on other planets.

Keywords: Atmospheric water vapor, climate system, planetary orbital variations, deep learning.

Main Text

In the solar system, as the Sun moves at high speed, the planets mutually influence

each other as well as their own internal structures, maintaining a dynamic balance. Earth's climate generally exhibits a relatively stable seasonal variation pattern, including the four seasons of spring, summer, autumn, and winter. This stability primarily results from the long-term evolution of Earth's orbit around the Sun and the orbital changes of other planets, and it is usually regarded as the norm of the Earth system[1-5]. Although the orbital variations of other planets in the solar system have little direct impact on Earth's climate, when different planets reach certain positions, the combined effects of these planets can exert specific influences on Earth's water cycle and climate change, thereby altering the normal patterns of internal climate change on Earth and even leading to natural disasters[6-9].

Through long-term astronomical and meteorological observations, it has been gradually discovered that changes in planetary orbits can sometimes have significant impacts on Earth's climate and environment, especially when specific alignments of different planetary orbits are more likely to trigger extreme weather and hydrological events[10-12]. In July 2005, Mercury and Venus were in orbits close to the Sun, whereas Earth and Mars were positioned further away. Jupiter was near Virgo in the ecliptic belt, Saturn was in Pisces, and Uranus and Neptune were in more distant orbits. Additionally, the Sun, Earth, and Moon were nearly aligned in a straight line. This unique celestial alignment triggered extreme tidal phenomena in the Bahamas, causing severe issues such as seawater intrusion and land erosion, and altered atmospheric water vapor levels[13-14]. In May 2006, a Mercury transit occurred, aligning the Sun, Mercury, and Earth in a straight line and resulting in severe flooding disasters in multiple regions globally, including Asia and Africa[15-17]. In July 2009, Mercury was near Leo, Venus orbited between the Sun and Earth, Mars was near Pisces, Jupiter was in Capricorn, and Saturn, Uranus, and Neptune were on the outer edges of the solar system. During the new moon phase in July 2009, the Moon positioned between the Earth and the Sun, a total solar eclipse of exceptionally long duration occurred over the Indian Ocean and parts of Southeast Asia, including China and Indonesia[18-19]. This astronomical phenomenon caused changes in local temperatures and water vapor, affecting plant and animal behavior[20-21]. This astronomical phenomenon caused changes in local temperatures and water vapor, affecting plant and animal behavior[22-23]. During this period, Africa, the Middle East, and parts of Asia experienced an exceptionally long annular solar eclipse. The Sun, Earth, and Moon were almost perfectly aligned, significantly enhancing tidal forces and affecting atmospheric water vapor content[24-27]. In March 2011, as the Moon neared the full moon phase, the Earth-Moon gravitational effects were enhanced. Mercury was in Aquarius, Venus in Aries, Mars in Pisces, and the outer planets Jupiter, Saturn, Uranus, Neptune, and Pluto were moving away from Earth. Simultaneously, the Sun, Moon, and Earth were nearly in a straight line, further intensifying tidal phenomena and causing rare extreme tidal events in coastal areas like Tokyo Bay. This resulted in widespread inland flooding and affected atmospheric water vapor changes[28-29]. In April 2014, Jupiter and Saturn were in close proximity in their orbits, coinciding with annular and total solar eclipses. This collectively affected regions of the South Pacific, Asia, Australia, and parts of the Americas[30-31]. Concurrently, active solar storms further exacerbated space weather anomalies. These events reflect the significant impact of planetary orbital changes on Earth's hydrological environment and climate change[32-33].

In recent years, this trend has remained notable. In March 2018, the northeastern United States experienced a powerful "bomb cyclone." At that time, the Sun was in Pisces in the ecliptic belt near the vernal equinox, and the Moon was in an elliptical

orbit near its perigee. This enhanced gravitational forces, significantly affecting Earth's tides, resulting in increased ocean tidal amplitudes and causing severe coastal floods and seawater inundation in areas such as Boston[34-35]. Additionally, Jupiter was in Libra, while Saturn and Mars were in Sagittarius. These astronomical factors collectively intensified tidal phenomena and extreme weather events. In November 2019, a Mercury transit occurred for the first time since 2006, with Mercury passing across the solar disk from Earth's perspective, appearing as a small black dot. This event caused an unprecedented rise in water levels in Venice, Italy, further exacerbating the city's flood risk and subsequently affecting atmospheric water vapor changes[36-37]. In May 2021, Venus and Mercury were very close within the ecliptic belt, undergoing a conjunction. During this period, the Thames River in London experienced a sharp rise in water levels, leading to floods in some low-lying areas[38-40]. In April 2023, Mercury was in Pisces and Venus in Aries, both near the Sun; Mars was in Gemini on the opposite side of Earth; Jupiter was in Pisces, and Saturn was in Aquarius. A rare hybrid solar eclipse occurred on the western coast of Australia, with the Sun, Moon, and Earth almost perfectly aligned. The overlap of a total solar eclipse and an annular solar eclipse enhanced the Moon's gravitational effect on tides. This collectively caused abnormal tidal fluctuations and noticeable tidal anomalies in coastal regions[41-43]. Notably, in October 2024, Mercury was in Libra and Venus in Scorpio, both close to the Sun. The Sun, Earth, and Moon were almost aligned in a straight line, and the Moon was at perigee (its closest point to Earth), significantly enhancing tidal forces[44-46]. These astronomical phenomena caused tidal effects to peak, especially in East Asia, where an abnormal astronomical high tide occurred during the autumn tides. Multiple coastal cities in China experienced widespread flooding, with infrastructure in some areas severely damaged and residents forced to evacuate urgently. These astronomical observations and extreme meteorological disaster events demonstrate the complex interactions between planetary orbital changes and Earth's climate and hydrological systems[47-50]. Although regular variations in planetary orbits have relatively minor and often overlooked effects on Earth, the superimposition of different planetary orbits can sometimes significantly impact the Earth system. This occurs through the mutual enhancement of gravitational and tidal forces, leading to extreme weather events and related disasters, and affecting changes in Earth's atmospheric water vapor content.

Some individuals have gradually recognized that the superimposed effects of different planets in the solar system, moving at high speeds and maintaining dynamic equilibrium, can sometimes trigger extreme natural disasters on Earth. Therefore, studying how changes in the orbits of different planets within the solar system affect Earth's climate, particularly the water cycle and ecosystems, is extremely important and represents an entirely new research direction. Due to the relatively regular changes in the relative positions of the Earth, Moon, and Sun, this study treats these three celestial bodies as an independent integrated system. In contrast, the orbital changes of other planets in the solar system relative to Earth's position are comparatively complex; thus, the orbital variations of these other planets are considered as a single collective factor in this study. To eliminate interference caused by internal changes within the Earth, this research employs the neighboring difference (differential) method, focusing specifically on the impact of orbital changes of different planets on Earth's atmospheric water vapor variations. Building on this, a series of dynamic quantitative models were constructed using comprehensive analytical methods such as Fourier transform, Multi-Taper Method (MTM) for multiple time-scale analysis, the Levenberg–Marquardt least squares optimization algorithm, harmonic decomposition techniques, weighted data fusion analysis, and adaptive sliding window techniques. These models aim to evaluate

and quantify the influence and contribution of orbital changes of different planets on Earth's atmospheric water vapor variations. Furthermore, by applying artificial intelligence deep learning models, this study predicts future atmospheric water vapor changes on Earth.

Figure 1 shows the technical road map used to analyze, quantify, and predict the impact of planetary orbital changes on Earth's atmospheric water vapor variations. Figure 1A is a planar schematic diagram of the orbital motions of various planets in the solar system. Centered on the Sun, the diagram details Earth's rotation, the Moon's revolution around Earth, Earth's revolution around the Sun, and the orbits of other planets around the Sun. These different planetary orbital changes affect Earth's atmospheric water vapor variations on different time scales. In Figure 1B, we analyzed data across different time scales to examine the impact of Earth's rotation on the daily variations of atmospheric water vapor, the changes induced by the Moon's orbit around Earth during the sidereal month, and the seasonal variations resulting from Earth's revolution. Additionally, orbital changes of other planets within the solar system also affect Earth's atmospheric water vapor variations. However, because these planets are relatively distant from Earth, their influence is comparatively minor, mainly reflected in the local details where the orbital signals of different planets overlap. The relative motions between other planets and Earth are complex and have longer periods, leading to diversity in the local detailed changes of Earth's atmospheric water vapor. The influences of orbital variations with longer periods from other planets mainly manifest on interannual and longer time scales; therefore, we consider their effects together in a comprehensive manner. These factors work together to influence the variations of Earth's atmospheric water vapor. By comprehensively analyzing atmospheric water vapor data across different time scales, we studied the impacts of different planetary orbital changes on Earth's atmospheric water vapor variations (see Section 2 of the Methods for details).

In Figure 1C, when describing the impact of Earth's rotation on changes in Earth's atmospheric water vapor, since the overall internal changes within Earth over two consecutive hours are relatively stable, and the periods of influence of Earth's revolution, the Moon's revolution, and other planetary orbital changes on Earth's atmospheric water vapor variations are longer compared to that of Earth's rotation, the variations over short timescales (e.g., within two hours) are relatively minimal. Based on this, we subtract atmospheric water vapor values between adjacent hours to approximately eliminate Earth's internal variability (such as CO_2 variations) and the influences of other longer-period planetary orbits. Consequently, we approximate the influence of Earth's rotation, represented by the harmonic function $Y_1(t)$. Since Earth's rotation period is 24 hours—completing its own rotation cycle within a day—and on the same day, Earth's revolution around the Sun accounts for only 1/365 of its annual orbital period. Additionally, the influence periods of other planetary orbital changes on Earth's atmospheric water vapor variations are extremely long. Therefore, when describing the influence of the Moon's revolution on Earth's atmospheric water vapor variations, we can approximately eliminate the effects of Earth's rotation (having completed a rotational period), Earth's revolution around the Sun, other planetary orbital influences, and Earth's internal variations by subtracting data from adjacent days within a sidereal month cycle. Consequently, we approximately obtain the influence of the Moon's revolution on Earth's atmospheric water vapor variations, represented by the irregular variation function $Y_2(t)$. Similarly, in each sidereal month, since Earth's

rotation and the Moon's revolution have both completed their respective orbital cycles, and the influence periods of other planetary orbits are extremely long compared to Earth's revolution period, we subtract the monthly averages of adjacent months between sidereal months to eliminate the effects of Earth's rotation, the Moon's revolution, other planetary orbital changes, and Earth's internal influences. This approach approximately obtains the effect of Earth's revolution on Earth's atmospheric water vapor variations, represented by the function $Y_3(t)$.

Although the orbital changes of other planets (such as Mercury, Mars, Jupiter, etc.) also simultaneously affect the variations in Earth's atmospheric water vapor, the magnitude of these orbital changes is very small on short time scales. Consequently, their impact on Earth's atmospheric water vapor is much smaller compared to the effects of Earth's revolution around the Sun, the Moon's revolution around Earth, and Earth's rotation. Therefore, we can approximately eliminate the influence of other planets' orbits through the method of neighboring subtraction. When analyzing the impact of other planets' orbital changes on variations in Earth's atmospheric water vapor, we smartly utilize the characteristics of Earth's rotation, the Moon's revolution, and Earth's revolution, each completing their respective orbital cycles within the interannual time scale. By employing pairwise subtraction, we can eliminate the effects of Earth's rotation, the Moon's revolution, Earth's revolution, and internal factors of Earth, thus obtaining the impact of other planets' orbital changes on Earth's atmospheric water vapor variations. We represent the combined influence of the orbital changes of other planets in the solar system (excluding Earth, the Moon, and the Sun) on Earth's atmospheric water vapor variations using the function $X(t)$. To gain a deeper understanding of how these planetary orbital changes affect Earth's atmospheric water vapor variations, we superimposed the function $X(t)$ onto the curves $Y_1(t) - Y_3(t)$ for analysis, constructing a series of mathematical models based on adjacent differences (differential method). The purpose of these models is to quantify the specific contributions of different planetary orbital changes to Earth's atmospheric water vapor variations on different time scales. With the help of the quantitative models proposed in this study, we can assess the extent to which different planetary orbital changes affect atmospheric water vapor variations (for detailed quantitative methods and formulas, see Section 3 of the Methods). Finally, in Figure 1D, we employed a Long Short-Term Memory (LSTM) deep learning model to construct predictive models on different time scales. After adjusting relevant parameter settings for training and cross-validation analysis, we further predicted future changes in Earth's atmospheric water vapor (see Section 4 of the Methods for details).

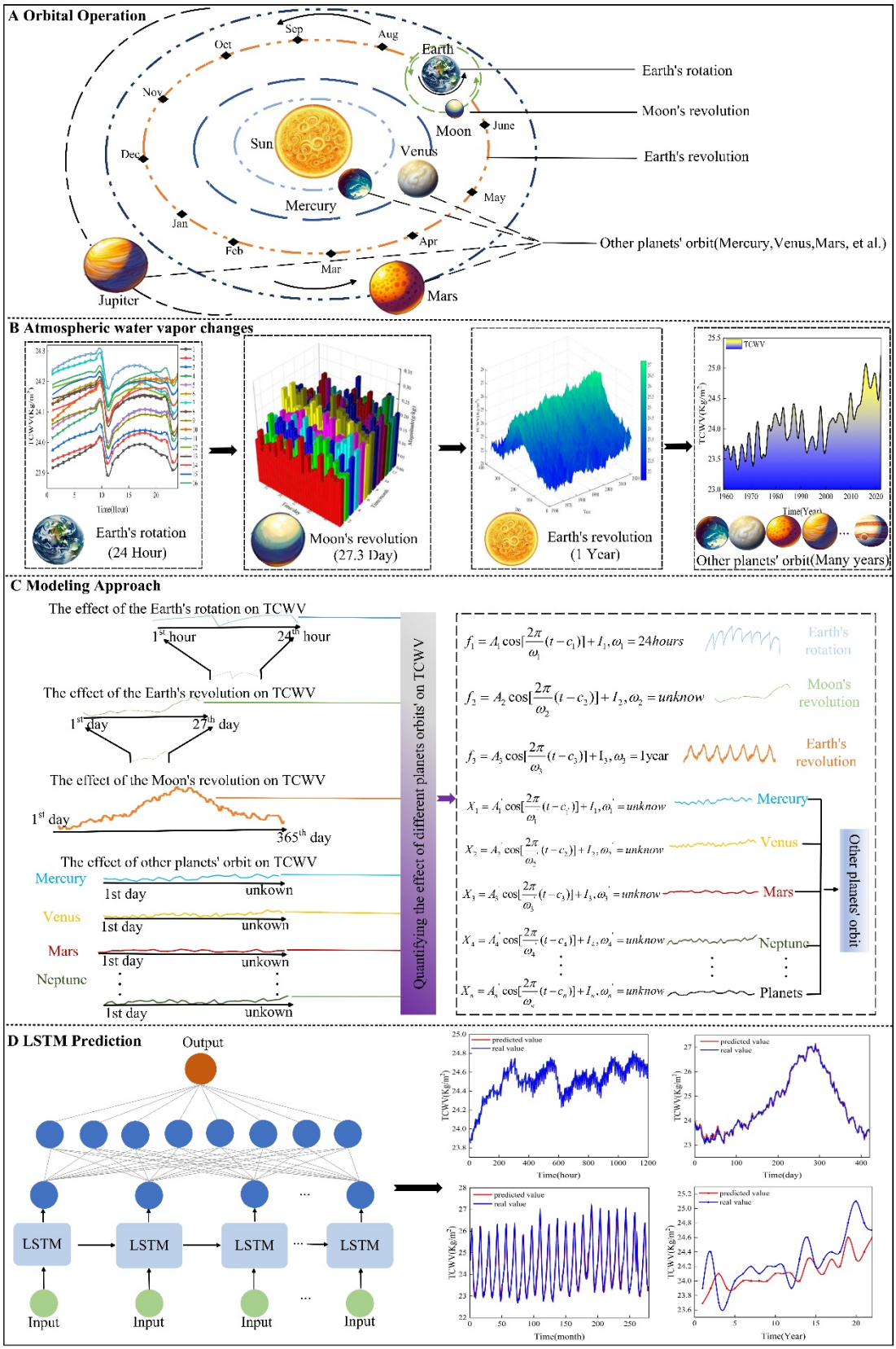

Figure 1. Technical road map for the analysis, quantification, and prediction of the impact of different planetary orbital changes on Earth's atmospheric water vapor variations. (A) Planar diagram of the main planetary orbital changes within the solar system. (B)Orbital Variations of Different Planets Dominate Earth's Atmospheric Water Vapor Changes Across Various Time Scales. (C) Construction of quantitative models for the impact of different planetary orbital changes. (D) LSTM deep learning prediction model and analysis.

Results

The Impact of Different Planetary Orbital Changes on Earth's Atmospheric Water Vapor Variations

Data analysis shows that variations in Earth's atmospheric water vapor content on different time scales are not only closely related to Earth's own motion but are also influenced by the orbital changes of other planets (see Methods Section 2). During Earth's rotation, the uneven distribution of land and sea leads to differences in surface albedo, thereby affecting the diurnal variations of Earth's atmospheric water vapor. Since Earth completes one rotation cycle every day, the diurnal variation trend of its atmospheric water vapor exhibits significant regularity and consistency (see Methods Section 2.1). Although the overall trend of Earth's atmospheric water vapor diurnal variation is similar, within a sidereal month cycle, the specific fluctuation values (vertical axis) of its daily variation trend are not consistent, and this difference is mainly dominated by the Moon's revolution. Furthermore, by analyzing the variations in atmospheric water vapor content within a sidereal month cycle, the Moon's declination(δ), the Earth-Moon distance, and the time series changes in Earth's rotation speed, we found further evidence of the Moon's revolution's impact on atmospheric water vapor. The study shows that the Moon's gravitational force induces atmospheric tides with periods of 27.3 days and 13.6 days, and the Moon's declination and Earth-Moon distance indirectly affect changes in atmospheric water vapor by influencing Earth's rotation speed (see Methods Section 2.2).

Moreover, within adjacent sidereal months, there is no fixed pattern in the specific fluctuation values of the atmospheric water vapor diurnal variation. Long-term data analysis found that this phenomenon is widespread. This is because, after the Moon completes one full revolution around Earth, Earth has also completed approximately 1/13 of its revolution around the Sun, while the orbits of other planets have also undergone changes. This causes a shift in the baseline at the start of the next month, resulting in the daily cycle variations associated with the Moon's orbit not being entirely consistent each month (if we assume that the Earth does not revolve and the orbits of other planets remain unchanged, considering only Earth's rotation and the Moon's revolution, then the Moon's daily influence cycles would be similar each month). The revolution of the Earth around the Sun leads to seasonal and latitudinal variations in solar radiation, which in turn also affects changes in atmospheric water vapor content. This process is also related to the positional changes of the Sun relative to Earth's equatorial plane, affecting Earth's rotation speed and leading to seasonal effects. Notably, within one revolution period, the variation of the monthly average atmospheric water vapor caused by Earth's revolution presents a sinusoidal pattern, showing a trend of first increasing and then decreasing (see Methods Section 2.3). Additionally, further analysis of interannual data from 1959 to 2022 revealed that the orbital variations of other planets (excluding Earth's rotation, revolution, and the Moon's revolution) also influence atmospheric water vapor, and this effect has been continuously present. Through Fourier Transform and Multi-Taper Method (MTM) analysis, we found that the combined effects of other planetary orbits jointly influence Earth's atmospheric water vapor variations (see Methods Section 2.4).

In summary, the variations of Earth's atmospheric water vapor are continuously influenced by the superimposed effects of different planetary orbital changes. On different time scales, these influences clearly exhibit different dominant relationships: Earth's rotation dominates the hourly variation trend each day, the Moon's revolution

dominates the daily fluctuation values within a sidereal month cycle, Earth's revolution dominates the monthly fluctuation values between adjacent sidereal months, and the orbital changes of other planets dominate the interannual variations of Earth's atmospheric water vapor between adjacent years.

Quantification of the Impact of Planetary Orbital Changes on Earth's Atmospheric Water Vapor Variations

Combining the mathematical models constructed in this study (see Section 3 of the Methods) and historical atmospheric water vapor data, we aim to determine the contributions of different planetary orbital changes to Earth's atmospheric water vapor variations. Figure 2 illustrates the contribution rates of Earth's rotation, the Moon's revolution, Earth's revolution, and the orbital variations of other planets to atmospheric water vapor changes across different time scales from 1959 to 2022, as calculated by a mathematical model, and the respective contributions are 4%, 10%, 71%, and 15%. The impact of different planetary orbital changes on Earth's atmospheric water vapor variations, from largest to smallest, is Earth's revolution, other planetary orbital changes, the Moon's revolution, and Earth's rotation. Figure 3 illustrates the effects of different planetary orbital changes on Earth's atmospheric water vapor variations from 1959 to 2022. Specifically, Figures A to D represent Earth's rotation, the Moon's revolution, Earth's revolution, and other planetary orbits, respectively. In the figures, changes in Earth's atmospheric water vapor are indicated with different colors based on their kernel densities. During this period, the ranges of atmospheric water vapor variations caused by Earth's rotation (Figure 3A), the Moon's revolution (Figure 3B), Earth's revolution (Figure 3C), and other planetary orbits (Figure 3D) are 0.01kg/m²-0.04kg/m², 0.04kg/m²-0.10kg/m², 0.3kg/m²-0.6kg/m², and 0.1kg/m²-0.5 kg/m², with average values of 0.02kg/m², 0.06kg/m², 0.5kg/m², and 0.1kg/m², respectively.

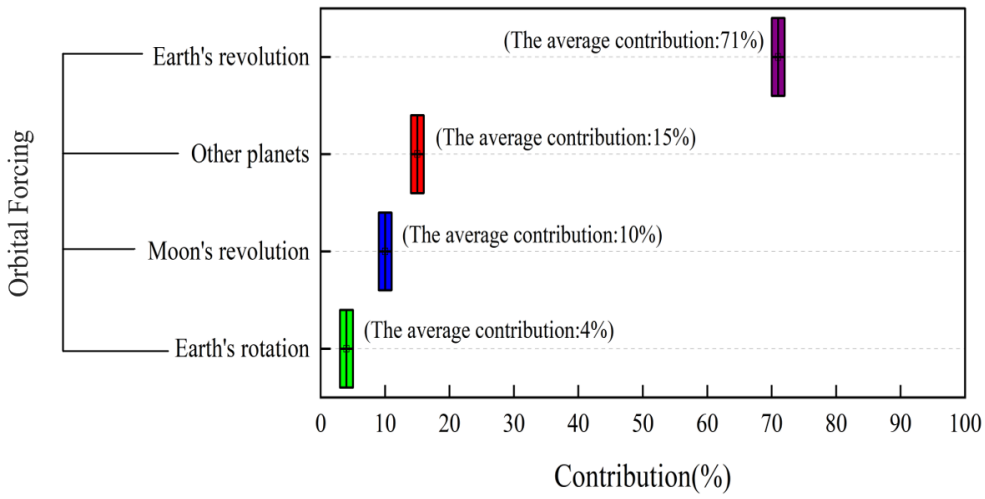

Figure 2. Average contributions of different planetary orbital changes to Earth's atmospheric water vapor variations from 1959 to 2022.

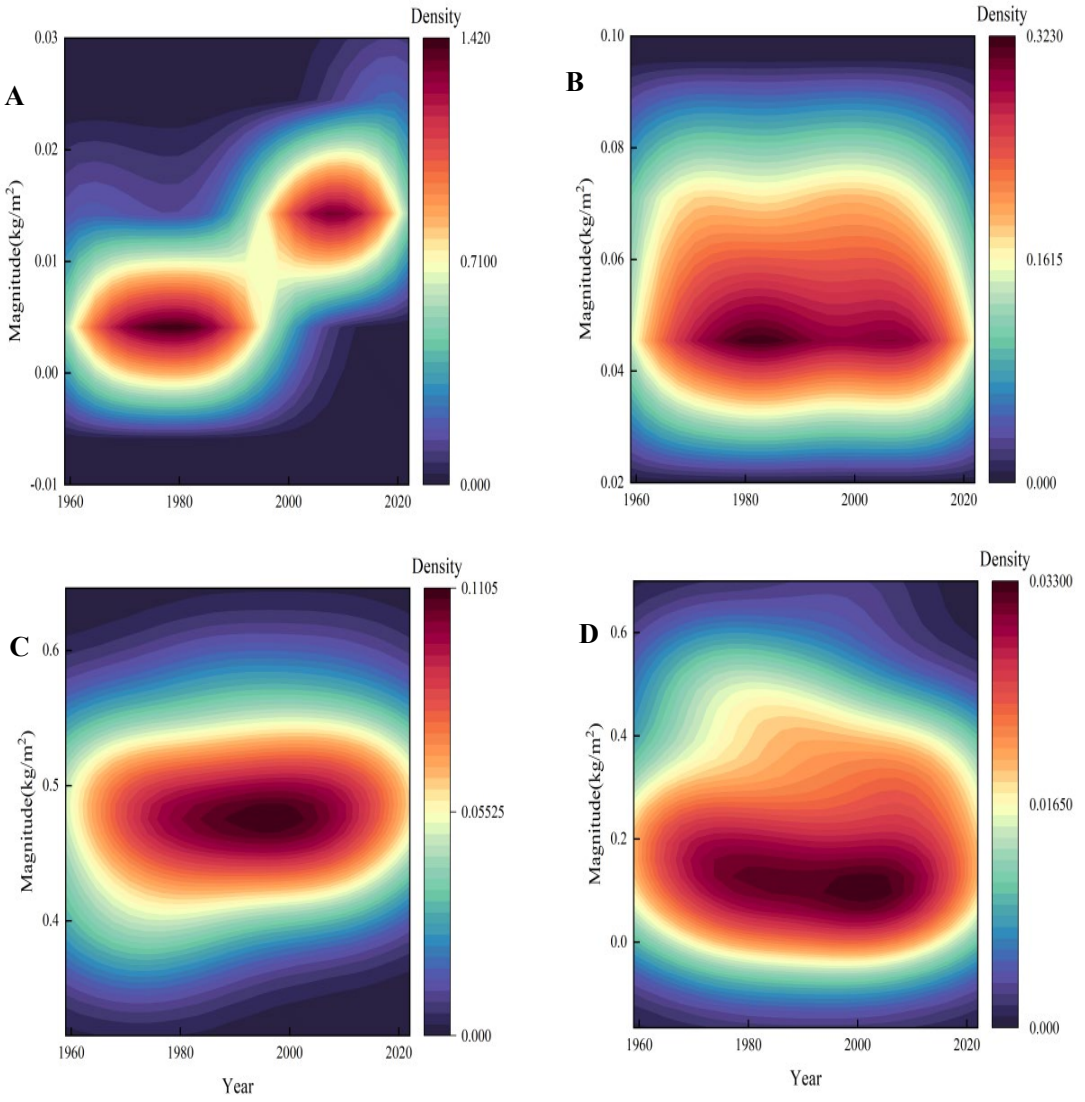

Figure 3. Kernel density plots showing the impact of different planetary orbital changes on Earth's atmospheric water vapor variations, with colors ranging from light to dark. (A) Impact of Earth's rotation. (B) Impact of the Moon's revolution. (C) Impact of Earth's revolution. (D) Impact of other planetary orbital changes.

Predicting future changes in water vapor in the Earth's atmosphere

In this study, we employed a Long Short-Term Memory (LSTM) deep learning model to predict future trends in Earth's atmospheric water vapor content (see Section 4 of the Methods for details). To ensure the accuracy of the predictions, we compared the performance of LSTM prediction models based on data at different time scales. When dividing the datasets, we selected hourly atmospheric water vapor data, daily average data, monthly average data, and yearly average data from 1959 to 2022. The data from 1959 to 2000 were used for model training, and data from 2000 to 2022 were used for model testing. In evaluating the predictive performance of the LSTM models, we particularly focused on metrics such as Mean Squared Error (MSE), Mean Absolute Error (MAE), and the R^2 statistic. Figure 4 and Table 1 respectively present the results of testing and validating the LSTM deep learning prediction model based on

atmospheric water vapor data across four different time scales (hourly data, daily average data, monthly average data, and yearly average data).

As can be seen in Figure 4, there are differences in the performance of the prediction models at different time scales. According to evaluation metrics such as R^2, the prediction performances for data at hourly, daily, and monthly scales are quite good, with R^2 values all exceeding 0.95, while the model performance at the yearly scale is relatively weaker. This reason can be explained by the laws governing planetary orbital motions. Variations on the hourly scale are primarily dominated by the influence of Earth's rotation, variations on the daily scale are mainly dominated by the influence of the Moon's revolution, variations on the monthly scale are primarily dominated by the influence of Earth's revolution around the Sun, and variations on the interannual scale are mainly dominated by the influence of orbital variations of other planets. Since Earth's rotation, the Moon's revolution, and Earth's revolution all have clear patterns, the prediction results are very good. The slightly poorer performance of the interannual scale model is due to the longer orbital periods of other planets (such as Venus, Mars, Mercury, Saturn, and Jupiter), leading to multiple overlapping influences that prevent the formation of significant periodic patterns in the short term. The laws of planetary orbital movements are consistent with the actual data analysis results.

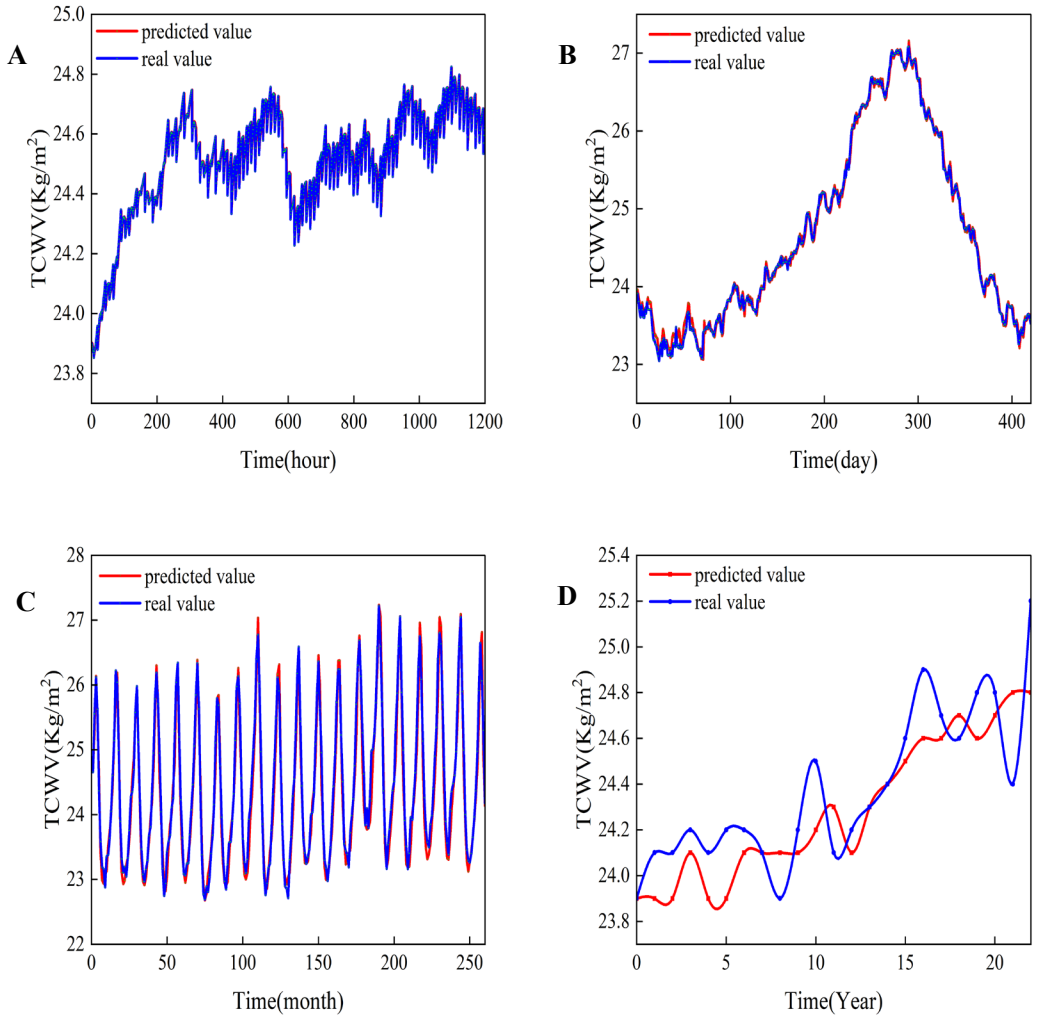

Figure 4. Prediction results of Earth's atmospheric water vapor under models at different time

scales (blue curve represents actual values, red curve represents predicted values). (A) Prediction of hourly average atmospheric water vapor (1200hours,2022year,1th-50th days). (B) Prediction of daily average atmospheric water vapor (420days,2021year,1th-2022,55th days). (C) Prediction of monthly average atmospheric water vapor (280months,2000-2022 years). (D) Prediction of yearly average atmospheric water vapor (22 years,2000-2022 years).

Table 1. Evaluation of LSTM model Predictions for Earth's Atmospheric Water Vapor Content Changes

Earth Atmospheric Water Vapor	Evaluation Metric	Hourly Scale	Daily Scale	Monthly Scale	Annual Scale
Model Evaluation	MAE	0.0195	0.0485	0.1866	0.0766
	MSE	0.0016	0.0037	0.0539	0.2166
	RMSE	0.0405	0.0608	0.2322	0.2768
	R^2	0.9682	0.9573	0.9511	0.5146

Finally, in Figure 5A, we uniformly applied the data from the four-time scales to the LSTM deep learning model to predict the annual average values. After comparing the results with the original annual average atmospheric water vapor, we found that the prediction performance of the monthly scale data model was the best, followed by the daily scale, hourly scale, and yearly scale data models. Taking into comprehensive consideration the influence of planetary orbits and the predictive accuracy of the model, we have chosen an LSTM model based on monthly-scale data to predict the interannual variation trends of Earth's future atmospheric water vapor content. Figure 5B presents the predicted annual average atmospheric water vapor from 2023 to 2032. In the Figure 5B, the red portion on the left represents the annual average atmospheric water vapor data from 1959 to 2022, the green portion is the predicted values from 2023 to 2032, and the blue curve is the fitted curve of water vapor data from 1959 to 2032. From Figure 5B, it can be seen that over the next decade, although Earth's atmospheric water vapor content will experience fluctuations, both the overall trend and the fitted curve display a slow upward trend. This trend is primarily attributed to the combined effects of orbital changes of different planets and internal variability, which continuously influence atmospheric water vapor.

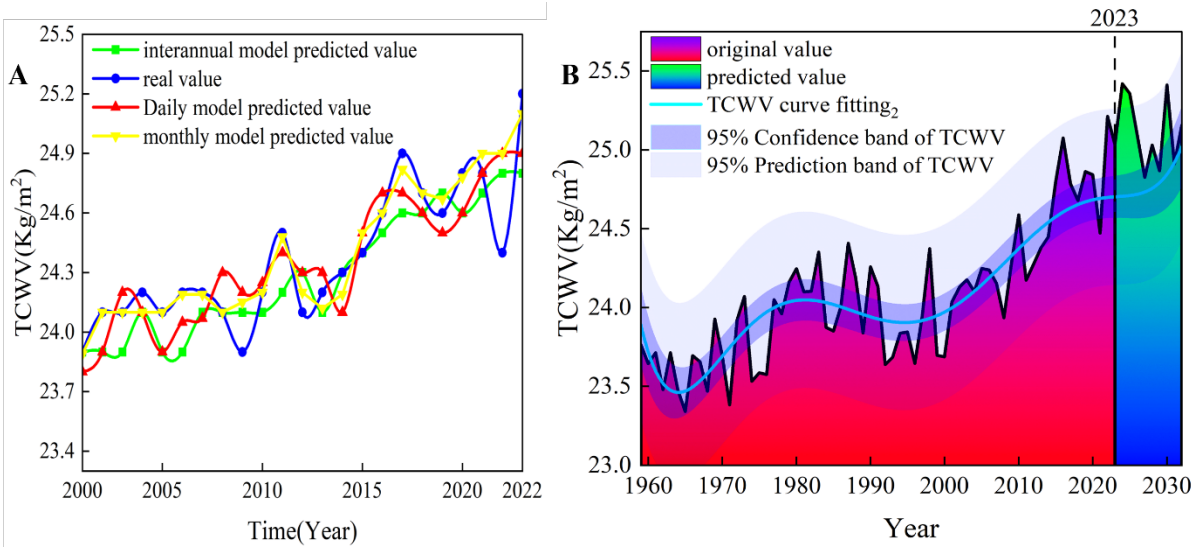

Figure 5. Prediction results of the LSTM deep learning model for Earth's interannual atmospheric water vapor variations. (A) Comparison of annual average predictions of Earth's atmospheric water

vapor using data from different time scales with the original annual average atmospheric water vapor data. (B) Prediction of changes in Earth's annual average atmospheric water vapor from 2023 to 2032 under the influence of planetary orbital changes.

Through in-depth analysis of long-term data and quantitative model predictions, this study reveals the significant impact of orbital variations of different planets on Earth's atmospheric water vapor content, particularly demonstrating their importance in understanding and predicting global climate change. Our research has found a close relationship between Earth's water vapor cycle and planetary orbital changes, providing new perspectives and theoretical support for constructing more precise climate models in the future. These findings are not only crucial for deeply understanding the complexity of Earth's climate system but also provide scientific evidence for formulating long-term climate change response strategies and environmental policies. Future research should further explore other potential influencing factors and validate and optimize models and predictions on broader temporal and spatial scales. Through these efforts, we will be able to more comprehensively understand the long-term impacts of planetary orbital changes on Earth's climate system, thereby more effectively addressing the challenges of global climate change.

Reference

1. Hays JD, Imbrie J, Shackleton NJ. Variations in the Earth's orbit: Pacemaker of the Ice Ages. *Science*, 1976, 194, 1121–1132.
2. Milankovitch M. Canon of insolation and the ice-age problem. *Belgrade*, 1941.
3. Berger AL. Long-term variations of daily insolation and Quaternary climatic changes. *Journal of the Atmospheric Sciences*, 1978, 35, 2362–2367.
4. Sussman GJ, Wisdom J. Chaotic Evolution of the Solar System. *Science*, 1992, 257, 56–62.
5. Eddy JA. The Maunder Minimum. *Science*, 1976, 192, 1189–1202.
6. Tardif D, et al. Orbital variations as a major driver of climate and biome distribution during the greenhouse to icehouse transition. *Science Advances*, 2021, 7, eabh2819.
7. Ruddiman WF. Orbital changes and climate. *Quaternary Science Reviews*, 2006, 25, 3092–3112.
8. Charney JG, Shukla J. Monsoon dynamics: Predictability of monsoons. *Journal of Geophysical Research*, 1981, 103, 14451–14510.
9. Webster PJ, Magafia VO, Palmer TN, et al. Monsoons: Processes, predictability, and the prospects for prediction. *Journal of Geophysical Research*, 1998, 103, 14451–14510.
10. Hunt B. The effects of past variations of the Earth's rotation rate on climate. *Nature*, 1979, 281, 188–191.
11. Williams G. Effects of the Earth's rotation rate on climate. *Nature*, 1980, 286, 309–310.
12. Trenberth KE, Fasullo J, Smith L. Trends and variability in column-integrated atmospheric water vapor. *Climate Dynamics*, 2005, 24, 741–758.
13. Hearty PJ, Tormey BR. Sea-level change and superstorms; geologic evidence from the last interglacial (MIS 5e) in the Bahamas and Bermuda offers ominous prospects for a warming Earth. *Marine Geology*, 2017, 390, 347–365.
14. Sahoo B, Jose F, Bhaskaran PK. Hydrodynamic response of the Bahamas archipelago to storm surge and hurricane-generated waves–A case study for Hurricane Joaquin. *Ocean Engineering*, 2019, 184, 227–238.
15. Tomar, M. S. An insight into the severe floods in India during 2005, 2006 & 2007. *Mausam, 63*(1), 2012, 65–70.
16. Singh, O., & Kumar, M. Flood events, fatalities and damages in India from 1978 to 2006. *Natural Hazards, 69*(3), 2013,1815–1834.
17. Kimuli, J. B., Di, B., Zhang, R., et al. A multisource trend analysis of floods in Asia-Pacific 1990–2018: Implications for climate change in sustainable development goals. *International Journal of Disaster Risk Reduction,* 2021, *59*, 102237.
18. Peñaloza-Murillo, M. A., & Pasachoff, J. M. Cloudiness and solar radiation during the longest total solar eclipse of the 21st century at Tianhuangping (Zhejiang), China. *Journal of Geophysical*

Research: Atmospheres, 2018, *123*, 13,443–13,461.

19. Marty, J., Dalaudier, F., Ponceau, D., et al. Surface pressure fluctuations produced by the total solar eclipse of 1 August 2008. *Journal of the Atmospheric Sciences,* 2013,*70*(3), 809–823.

20. Becklin, K. M., Anderson, J. T., Gerhart, L. M., et al. Examining plant physiological responses to climate change through an evolutionary lens. *Plant Physiology,* 2016, *172*(2), 635–649.

21. Ding, F., Wan, W., Ning, B., et al. GPS TEC response to the 22 July 2009 total solar eclipse in East Asia. *Journal of Geophysical Research,* 2010, *115*, A07308.

22. NASA. 2010. *Annular Solar Eclipse of January 15, 2010*. NASA Solar System Exploration. Retrieved from https://eclipse.gsfc.nasa.gov/SEplot/SEplot2001/SE2010Jan15A.GIF

23. Le, H., Liu, L., Ding, F., et al. Observations and modeling of the ionospheric behaviors over the East Asia zone during the 22 July 2009 solar eclipse. *Journal of Geophysical Research,* 2010, *115*, A10321.

24. Voulgaris, A. G., Gaintatzis, P. S., Seiradakis, J. H., et al. Spectroscopic coronal observations during the total solar eclipse of 11 July 2010. *Solar Physics,* 2012, *278*(1), 187–202.

25. Ratnam, M. V., Eswaraiah, S., Leena, P. P., et al. Effect of the annular solar eclipse of 15 January 2010 on the low latitude mesosphere. *Journal of Atmospheric and Solar-Terrestrial Physics,* 2012, *80*, 340–346.

26. Dutta, G., Kumar, P. V., Ratnam, M. V., et al. Response of tropical lower atmosphere to annular solar eclipse of 15 January, 2010. *Journal of Atmospheric and Solar-Terrestrial Physics,* 2011, *73*(13), 1907–1914.

27. Scafetta, N. High resolution coherence analysis between planetary and climate oscillations. *Advances in Space Research,* 2016, *57*(10), 2121–2135.

28. Hisamatsu R, Tabeta S, Kim S, et al. Storm surge risk assessment for the insurance system: A case study in Tokyo Bay, *Japan. Ocean & Coastal Management*, 2020, 189, 105147.

29. Uehara K, Saito Y. Tidal amplitude decreases in response to estuarine shrinkage: Tokyo Bay during the Holocene. Estuarine, *Coastal and Shelf Science*, 2019, 225, 106225.

30. NASA. 2014. *Annular Solar Eclipse of April 29, 2014*. NASA Solar System Exploration. Retrieved from https://eclipse.gsfc.nasa.gov/SEplot/SEplot2001/SE2014Apr29A.GIF

31. Mares, I., Dobrica, V., Mares, C., et al. Assessing the solar variability signature in climate variables by information theory and wavelet coherence. *Scientific Reports,* 2021, *11*, 11337.

32. Tobian, A., Gerten, D., Fetzer, I., et al. Climate change critically affects the status of the land-system change planetary boundary. *Environmental Research Letters,* 2024, *19*(5), 054060.

33. Gray, L. J., Beer, J., Geller, M., et al. Solar influences on climate. *Reviews of Geophysics,* 2010, *48*(4), RG4001.

34. Sun Q, Dangendorf S, Wahl T, et al. Causes of accelerated high-tide flooding in the U.S. since 1950. *Climate and Atmospheric Science*, 2023, 6, 210.

35. Gori A, Lin N, Xi D, et al. Tropical cyclone climatology change greatly exacerbates U.S. extreme rainfall–surge hazard. *Nature Climate Change*, 2022, 12, 171–178.

36. Cavaleri L, Bajo M, Barbariol F, Bastianini M, et al. The 2019 flooding of Venice. *Journal of Coastal Research*, 2020, 33, 42–49.

37. Cavaleri L, Bajo M, Barbariol F, et al. The October 29, 2018 storms in Northern Italy – An exceptional event and its modeling. *Progress in Oceanography*, 2019, 178, 102178.

38. Inayatillah A, Haigh ID, Brand JH, et al. Digitising historical sea level records in the Thames Estuary, UK. *Scientific Data*, 2022, 9, 167.

39. Mikhailov VN, Mikhailova MV. Tides and storm surges in the Thames River Estuary. *Water Resources*, 2012, 39, 351–365.

40. Fan Y. Ensemble flood predictions for River Thames under climate change. *National Science Open*, 2024, 3, 20230027.

41. Aa E, Coster AJ, Zhang SR, et al. 2-D Total Electron Content and 3-D Ionospheric Electron Density Variations During the 14 October 2023 Annular Solar Eclipse. *Journal of Geophysical Research: Space Physics*, 2024, 129, 32447.

42. Gómez DD. Ionospheric Response to the December 14, 2020 Total Solar Eclipse in South America. *Journal of Geophysical Research: Space Physics*, 2021, 126, 7.

43. Mrak S, Semeter J, Nishimura Y, Hirsch M, Sivadas N. Coincidental TID Production by Tropospheric Weather During the August 2017 Total Solar Eclipse. *Geophysical Research Letters*, 2018, 45, 10903–10911.

44. Liu JY, Wu TY, Sun YY, et al. Lunar tide effects on ionospheric solar eclipse signatures: The

August 21, 2017 event as an example. *Journal of Geophysical Research: Space Physics*, 2020, 125, e2020JA028472.

45. Dong L, Liu J, Zhou J, et al. The influence of astronomical tide phases on urban flooding during rainstorms: Application to Macau. *Journal of Hydrology: Regional Studies*, 2024, 56, 101998.

46. Núñez P, Castanedo S, Medina R. A global classification of astronomical tide asymmetry and periodicity using statistical and cluster analysis. *Journal of Geophysical Research: Oceans*, 2020, 125, e2020JC016143.

47. Xu L. Relationships between the East Asian monsoon anomalous and the red tide occurrence frequency in the East China Sea mental factors in the Beidaihe waters of the Qinhuangdao. *Marine Forecasts*, 2013.

48. Popp, M., Eggl, S. Climate variations on Earth-like circumbinary planets. *Nature Communications*, 2017*, 8*, 14957.

49. Zherebtsov, G.A., Kovalenko, V.A., Kirichenko, K.E. The role of solar activity in observed climate changes in the 20th century. *Geomagn. Aeron, 2017,*57, 637–644.

50. Lee H, Kim J. Assessing the Impact of Celestial Mechanics on Global Climate Patterns Using Advanced Climate Models. *International Journal of Climate Science*, 2024, 39, 89–105.

Methods

1. Data

In this study, we used the fifth-generation global atmospheric reanalysis dataset (ERA5) provided by the European Centre for Medium-Range Weather Forecasts (ECMWF) to obtain atmospheric water vapor data. ERA5 combines model data with observations from around the world to create a global dataset[51-52]. The dataset has a temporal resolution of 1 hour and a spatial resolution of 0.25°×0.25°. We utilized data from January 1959 to December 2022 to analyze the impact of different planetary orbital changes on Earth's atmospheric water vapor variations at different time scales.

In addition, to enhance the depth and breadth of our analysis, we collected supplementary auxiliary data[53-54]. These include daily Length of Day (LOD) data provided by the International Earth Rotation and Reference Systems Service (IERS) Prediction Center of the U.S. Naval Observatory, and daily atmospheric carbon dioxide concentration data from 1959 to 2022 archived by the Scripps Institution of Oceanography. Meanwhile, we obtained lunar phase information from Switzerland's Fourmilab website and daily data on the Earth-Sun distance, solar declination angle, and lunar declination angle from the ephemerides of NASA's Jet Propulsion Laboratory (JPL). These auxiliary datasets provide comprehensive background information, greatly improving the accuracy of our analysis of Earth's atmospheric water vapor trends.

2. The Impact of Different Planetary Orbital Changes on Earth's Atmospheric Water Vapor Variations

2.1 The Impact of Earth's Rotation on Earth's Atmospheric Water Vapor Variations

During Earth's rotation, we observe that atmospheric water vapor exhibits different changes within a single day. Taking the 2021 vernal equinox as an example, we studied the impact of Earth's rotation on the amount of solar radiation received, as well as the impact of changes in Earth's land-sea distribution on the distribution of atmospheric water vapor. Analysis of data from the 2021 vernal equinox indicates that we observed significant hourly variations in Earth's atmospheric water vapor values, particularly during Coordinated Universal Time (UTC) 10–11 and UTC 22–23 (Figure S1A). These changes are closely related to the movement of the Earth's regions illuminated by the Sun. Due to Earth's rotation, the solar zenith position moves westward by approximately 15°every hour, leading to changes in the geographic areas covered by solar radiation at different times on the vernal equinox. For example, at UTC 11:00, the Sun primarily illuminates most parts of Asia and Europe, Africa, Oceania, as well as the Indian and Atlantic Oceans (Figure S1B). At UTC 21:00, the irradiated regions shift to parts of North America, South America, portions of the Asian and European continents, and also cover parts of the Pacific and Atlantic Oceans (Figure S1C). By analyzing the spatial distribution of atmospheric water vapor in Figures S1D and S1E, we can observe that atmospheric water vapor varies with time and geographical location. Due to rotation, different regions on Earth receive different amounts of solar radiation at different times, and the differences in land-sea distribution further lead to variations in the Earth's internal feedback mechanisms, thereby affecting the diversity of atmospheric water vapor distribution.

Figure S2A displays the changes in Earth's atmospheric water vapor over a

consecutive 16-day period from January 1 to January 16, 2017. The waveforms of the curves show a high degree of similarity, and the patterns of hourly variations are basically consistent, which is closely related to Earth's daily rotation. Figure S2B reveals the hourly variation trends of Earth's atmospheric water vapor for each day throughout 2017, while Figures S2C and S2D enlarge and display local details within the annual data. These images indicate that the variation trends of Earth's atmospheric water vapor are consistent throughout the year. Analysis of long-term data from 1959 to 2022 further confirms the universality of this phenomenon, showing that atmospheric water vapor exhibits consistent daily periodic variations during Earth's rotation. Figures S3A, S3B, S3C, and S3D respectively display the daily average atmospheric water vapor changes at seasonal nodes (vernal equinox, summer solstice, autumnal equinox, winter solstice) from 1959 to 2022 (the variations are similar each year; see Figure S10 for details), further revealing the hourly dynamic variation patterns of Earth's atmospheric water vapor. These data indicate that regardless of seasonal changes, Earth's atmospheric water vapor follows a cyclical pattern within a day: first increasing, then decreasing, increasing again, and finally decreasing. Additionally, an analysis was conducted on the differences in Earth's atmospheric water vapor data between every two adjacent hours within each day from 1959 to 2022. The study found that the waveforms of these data differences exhibit consistency across any two consecutive days. Figures S3E, S3F, S3G, and S3H exemplify the daily average difference waveforms of Earth's atmospheric water vapor at seasonal nodes during the study period, showing that they have similar variation trends.

Through the analysis of hourly variations within consecutive days and long-term data, it was found that although Earth's position in its orbital revolution over two consecutive days, the Moon's position in its revolution around Earth, and the orbital positions of other planets all change, these variations have a relatively small impact on Earth's atmospheric water vapor within adjacent 24-hour periods. Therefore, it can be concluded that the hourly variations of Earth's atmospheric water vapor within a daily cycle are mainly due to the influence of Earth's rotation.

2.2 The Impact of the Moon's Revolution on Earth's Atmospheric Water Vapor Variations

The periodic variation in the Moon's gravitational influence on Earth's atmospheric water vapor induces atmospheric tides with periods of 27.3 days and 13.6 days, and also affects weather changes. The tidal effects caused by the Moon and their periodic variations are well-known phenomena and can be clearly observed in oceanic records. The lunar tidal period is generated by the gravitational effects of the Moon on Earth, which, to some extent, regulate ocean currents, thereby directly and indirectly influencing the spatial distribution of Earth's atmospheric water vapor[55-59]. The asymmetric alternating changes in the Moon's gravitational pull-on Earth's solid body and oceans lead to periodic oscillations in crustal stress. These periodic oscillations may trigger local natural disasters and affect water vapor variations locally and even globally. Additionally, changes in Earth's atmospheric water vapor are influenced by the Moon's reflection and infrared radiation[60-66]. Therefore, the impact of the Moon's revolution on Earth's atmospheric water vapor variations cannot be ignored.

Figure S4A shows the changes in Earth's atmospheric water vapor within a sidereal month cycle in 2017. From the figure, it can be seen that although the daily curves and fluctuation trends of Earth's atmospheric water vapor are similar, the specific numerical values (vertical axis) of the daily fluctuation trends are still changing. These variations

are mainly due to the influence of the Moon's revolution around the Earth. Specifically, the significant changes in the vertical coordinate every few days are determined by the Moon's position over different land and sea areas. Earth's rotation leads to the daily variation patterns of atmospheric water vapor, while the differences in data fluctuations from day to day are mainly due to the Moon's revolution affecting Earth's atmospheric water vapor. Analysis has revealed that this situation exists not only within a single sidereal month cycle.

Figure S4B takes 2017 as an example to show the daily average changes of Earth's atmospheric water vapor over 13 sidereal month cycles in that year. The analysis indicates significant differences in atmospheric water vapor variations within each sidereal month. Additionally, as shown in Figure S4C, Earth's atmospheric water vapor changes in different years (1979–1992) also exhibit certain fluctuations. Figure S4D further presents a three-dimensional plot displaying the daily average atmospheric water vapor fluctuations over 856 sidereal month cycles from 1959 to 2022. Based on hourly data from ERA5, the data is divided according to a 27.3-day cycle. To reduce the accumulation of periodic calculation errors, the hourly atmospheric water vapor values starting from 0:00 on January 1, 1959, are divided into specific intervals: 655 hours, 655 hours, 655 hours, 657 hours, 655 hours, 655 hours, 655 hours, 657 hours, 655 hours, and 656 hours. In the three-dimensional plot, only the daily average atmospheric water vapor values for the first 27 days of each sidereal month cycle are shown. It is evident that within each sidereal month cycle, the daily average atmospheric water vapor fluctuates significantly, and the variation trends over 856 sidereal month cycles are not the same. These irregular fluctuations within the sidereal month are primarily caused by variations in gravitational forces resulting from the Moon's revolution around the Earth.

Moreover, by analyzing the distance between the Moon and Earth, the daily lunar declination angle (δ), and changes in Earth's rotation speed from 1959 to 2022, we found further evidence of the Moon's revolution impacting Earth's daily atmospheric water vapor. In this study, the daily Length of Day (LOD) values are used to measure Earth's angular velocity. In astronomy, the lunar declination angle is defined as the angle between its apparent trajectory on the celestial sphere and the celestial equator. Figure S5A illustrates the inclination of the Moon's orbital motion relative to the celestial equator during its revolution around the Earth, presented as a schematic diagram. Taking 1979 as an example, Figure S5B shows the trend of Earth's daily average atmospheric water vapor in that year. Figure S5C displays the time series changes of daily lunar declination angle data and Earth's rotation speed data (LOD) over 13 sidereal months in that year. Figure S5D illustrates the temporal variations of the Length of Day (LOD) and the atmospheric water vapor difference (ΔTCWV) between two consecutive days. Figure S5E presents the temporal changes of the Moon's declination angle and the atmospheric water vapor difference (ΔTCWV) between two consecutive days. The trends in the changes of ΔTCWV and LOD over two consecutive days exhibit similar rising and falling patterns, indicating that Earth's rotation plays a role in influencing diurnal atmospheric water vapor variations. On the other hand, Section 2.1 of the Methods has already discussed the significant impact of Earth's rotation on daily atmospheric water vapor changes. Therefore, if Earth's rotation speed changes regularly with the Moon's movement, this would further prove that the Moon can indirectly influence Earth's daily atmospheric water vapor variations by affecting Earth's rotation.

During the study period (1959–2022), the variations in the Length of Day (LOD) consisted of two primary oscillations with periods of 27.3 days and 13.6 days, respectively. These two periods correspond to the Moon's sidereal cycles. By comparing Figures S5C and S5D, it can be observed that when the absolute value of the Moon's declination reaches its maximum, the LOD is at its minimum (orange arrows), and when the Moon's declination is zero, the LOD reaches its maximum (green arrows). Simultaneously, the LOD exhibits oscillations with periods of 13.6 days and 27.3 days, which are entirely consistent with the Moon's synodic month cycles. Generally, changes in the Moon's declination lead changes in the LOD by about one day. Moreover, analysis of the LOD oscillation curves reveals that the duration of sustained increases or decreases in LOD does not correspond to one quarter of the lunar cycle but instead varies between 5 and 9 days. All short-period (13 days) and long-period (14–15 days) LOD oscillations correspond respectively to the Moon's perigee (P) and apogee (A). According to Kepler's law of areas, when the Moon is farther from Earth, its orbital speed is slower, so the oscillation periods that include the apogee are slightly longer than those that include the perigee. This also indicates that the Moon's orbital speed around Earth affects changes in the LOD. At the same time, all peaks corresponding to perigee periods (P) are higher than those of adjacent apogee periods (A), indicating that the Moon's varying distance from Earth also influences the variations in LOD. When the perigee(P) is near the peak and closer to the new moon or full moon, the peak of the LOD cycle is the highest. Through the above analysis, it is clear that the Moon's revolution around Earth is one of the important reasons affecting the daily variations in Earth's atmospheric water vapor.

2.3 The Impact of Earth's Revolution on Changes in Earth's Atmospheric Water Vapor

In Earth's motion, Earth's revolution around the Sun is one of the important factors affecting changes in Earth's atmospheric water vapor. Earth's revolution causes periodic changes in the Sun's position relative to the equatorial plane. When Earth is at different positions on its elliptical orbit around the Sun, seasonal changes are formed[67-71]. Different seasons and regions receive varying amounts of solar radiation, directly influencing atmospheric temperature and the evaporation and precipitation of water vapor.

Figures S6A and S6B show the changes in Earth's atmospheric water vapor over two consecutive sidereal month cycles in 2017. By analyzing the data in detail, we found that due to Earth's rotation, the daily variation curves of atmospheric water vapor exhibit a high degree of similarity. Earth's rotation leads to the diurnal variation patterns of atmospheric water vapor, making its daily fluctuation curves relatively consistent. However, within a sidereal month cycle, due to the influence of the Moon's revolution, while Earth's atmospheric water vapor presents the same variation curves, the specific fluctuation values (vertical axis) of the upward and downward trends differ. This is because as the Moon revolves around Earth, it produces periodic tidal effects on Earth's atmospheric system, thereby affecting the distribution and variation of atmospheric water vapor. Within two consecutive sidereal months, the specific upward and downward fluctuation values of Earth's atmospheric water vapor also exhibit significant differences. Theoretically, the fluctuations of Earth's atmospheric water vapor over two sidereal month cycles should exhibit similar patterns under the gravitational influence of the Moon. However, in reality, significant differences are observed, primarily due to the influence of Earth's revolution. Since Earth completes 54⁄365 of its orbital

revolution period during two sidereal month cycles, its orbital motion has a considerable impact on the distribution of atmospheric water vapor. This leads to differences in the specific fluctuations of atmospheric water vapor during two consecutive sidereal months. Through the analysis of long-term data, we found that this phenomenon is universal—that is, within each sidereal month cycle, there are differences in specific numerical fluctuations (see Figure S4D).

Figure S6C, on the other hand, presents a graph of the trend of the Earth's atmospheric water vapor changes over 63 Earth rotation cycles between 1959 and 2022. From the figure, it can be seen that the changes of the Earth's atmospheric water vapor during the rotation cycles show regular fluctuations. Specifically, Earth's atmospheric water vapor first increases and then decreases within each cycle, forming a fluctuation curve analogous to a sine wave. This fluctuation is mainly attributed to the differences in the amount of solar radiation received by different seasons and regions during the Earth's revolution around the Sun, which in turn leads to seasonal changes in atmospheric temperature and water vapor content. For example, January and December are the time periods when the daily average value of water vapor in the Earth's atmosphere is the lowest, which is associated with weaker solar radiation, lower temperatures, and reduced evaporation of water vapor during the winter months, while August and September are the highest, which is closely related to strong solar radiation, higher temperatures, and increased evaporation of water vapor during the summer months. Earth's revolution induces seasonal changes, significantly affecting the distribution of atmospheric temperature and water vapor. These seasonal variations exhibit regular fluctuations, reflecting differences in the amount of solar radiation received indirectly across seasons and regions, which in turn leads to cyclical fluctuations in the Earth's atmospheric water vapor over the annual cycle. Figure S6D further illustrates some localized details in the sinusoidal fluctuations between years. These localized fluctuations are not completely regular, showing the ups and downs of the interannual midheaven variations, which are mainly affected by the superimposed effects of the Moon's rotation around the Earth and the changes in the orbits of other planets. The influence of the Moon's revolution on the diurnal variations of Earth's atmospheric water vapor has been thoroughly analyzed in Section 2.2 of the Methods. In contrast, gravitational perturbations from the orbits of other planets have produced complex superimposed effects on the distribution of Earth's atmospheric water vapor on longer time scales. The specific effects of the orbits of other planets on the variation of atmospheric water vapor on the Earth are explored in detail in the next section.

2.4 The Impact of Other Planetary Orbital Changes on Earth's Atmospheric Water Vapor Variations

Analysis in Sections 2.1, 2.2, and 2.3 of the Methods indicates that if the solar system consisted only of the Sun, Earth, and Moon, then the variations in Earth's atmospheric water vapor would exhibit relatively regular patterns. However, as shown in Figure S6D, there are still some differences in the local detailed variations of Earth's atmospheric water vapor. This is because, in addition to Earth's rotation, the Moon's revolution around Earth, and Earth's revolution around the Sun affecting atmospheric water vapor variations, other planets in the solar system also influence these changes. The orbital changes of these planets have longer periods, and they move simultaneously with Earth, causing the effects of their orbital changes to be superimposed on those of Earth's rotation, the Moon's revolution, and Earth's revolution. Since each planet has its unique periodicity, this leads to different characteristics of Earth's atmospheric water vapor at

different time scales. Moreover, the relationships among Earth, the Moon, and the Sun are relatively stable, and their motion patterns can be considered a relatively simple system—that is, one body orbiting another. In contrast, the relative motions between other planets and Earth are more complex, and the relative motions among planets further increase the complexity of how their orbital changes impact Earth's atmospheric water vapor. These orbital changes resulting from relative motion make it difficult to describe their periodic variation patterns using mathematical models in the short term.

To further illustrate this point, we collected and analyzed relevant data. Figure S7 shows the variations in Earth's atmospheric water vapor during the vernal equinox, summer solstice, autumnal equinox, and winter solstice for all the years in the study period. Analysis indicates that in Figure S7A, the trend of Earth's atmospheric water vapor changes on the vernal equinox is generally consistent each year, but local fluctuations still exist. This is because the primary influence within the daily cycle is determined by Earth's rotation, while the local variations are the result of the superimposed effects of orbital changes from other planets. By analyzing different data from Figures S7B to S7D, we can see that this similarity in variation exists every day. Due to the relatively long orbital periods of other planets and the complexity of their relative orbital trajectories with Earth, their influences cause the periodic fluctuations in Earth's atmospheric water vapor to primarily manifest on longer interannual time scales. Furthermore, the periodic regularities are not highly pronounced and are the result of combined effects. These superimposed influences of different planetary orbital changes lead to diversity and uncertainty in the local variations of Earth's atmospheric water vapor, thereby contributing to the diversity of climate change.

To conduct a more in-depth analysis of the impact of other planets' orbits on the superimposed signals of Earth's atmospheric water vapor, Fourier transform analysis[72-74] and the Multi-Taper Method (MTM)[75-76] were employed to analyze long-term time series data on interannual scales. This approach aims to achieve a more comprehensive understanding of the long-term effects of orbital changes of other planets on variations in Earth's atmospheric water vapor. The analysis utilized ERA5 reanalysis data spanning from 1959 to 2022. Spectral domain methods and harmonic approximation models were developed to identify all periodic oscillations in the historical time series and to reconstruct the impact of planetary orbital changes on Earth's atmospheric water vapor. By using frequency domain methods, we calculated the periods, amplitudes, and phases in the time series to extract relevant oscillation signals. Spectral analysis methods help identify the periodic components in the time series, thereby constructing harmonic approximation models. The set of oscillation signals P of the reconstruction model can be expressed by the following continuous-time equation:

$$\hat{P}_t = U + \sum_{m=1}^{M} A_m \sin(2\pi f_m (t - 1959) + \emptyset_m) \quad (1)$$

Where f, A and $\emptyset$ represent the frequency, amplitude, and phase of the sine wave, respectively, while t denotes the year, and M is the number of significant peaks extracted. When applying the FFT and MTM methods for frequency analysis, the U values are set to 0.013 and 0.0094, respectively. The planetary orbital change periods obtained from these two spectral analysis methods are listed in Tables S1 and S2. Figures S8 and S9 show the reconstructed information after decomposition based on the FFT and MTM methods, reflecting the impact of other planetary orbital changes on atmospheric water vapor variations. The research results indicate that since 1959, global atmospheric water vapor has exhibited multiple fluctuation periods, including 3.5 years, 8.25 years, 9.15

years, 9.85 years, 13.4 years, 15.25 years, 21.3 years, 32 years, and 62 years. These periods correspond to the astronomical periods of various combinations of planetary orbits; detailed analysis results can be found in Tables S1 and S2. This analysis indicates that the superimposed effects of different planetary orbits have influenced the variations in Earth's atmospheric water vapor. These periodic fluctuations cause interannual-scale changes in the climate system, influencing key climatic factors such as precipitation patterns, temperature, and atmospheric circulation.

3. Quantifying the Impact of Different Planetary Orbital Changes on Earth's Atmospheric Water Vapor Variations

3.1 Constructing the Quantitative Model

Theoretically, if Earth remains relatively stationary with respect to all other planets (i.e., the basis function of Earth's atmospheric water vapor variations remains stable), then the signal superposition effects caused by other planetary movements on Earth's atmospheric water vapor could be decomposed using Fourier transforms. However, due to Earth's revolution around the Sun, aside from the relatively stable relative motion trajectories between Earth and the Sun (elliptical) and Earth's rotation, the relative motion trajectories between Earth and other planets are highly complex. This means that, except for the Sun, the impact of other planets on Earth's atmospheric water vapor variations is extremely intricate because Earth's atmospheric water vapor itself is changing, and the influences of other planets are also changing. This complexity makes it difficult for Fourier transforms to systematically separate these signals. Therefore, based on the analysis in Section 2 of the Methods, we studied the impacts of different planetary orbital changes on Earth's atmospheric water vapor variations at different time scales. To quantify the impact of different planetary orbital variations on changes in Earth's atmospheric water vapor, we have developed a theoretical framework. In this study, Earth is considered an integrated system, with the natural variations of its internal climate system viewed as a response to planetary orbital forcing. Therefore, the primary changes in Earth's atmospheric water vapor can be seen as an intrinsic manifestation of orbital forcing. At the same time, subtracting adjacent values can minimize the influence of internal variations (such as CO_2) on Earth as much as possible. Based on this approach, we have constructed a series of dynamic quantitative models to analyze and quantify the effects of different planetary orbital variations on changes in Earth's atmospheric water vapor.

$$F(t) = Y_1(t) + Y_2(t) + Y_3(t) + X(t) \tag{2}$$

Where the function $F(t)$ represents the impact of all planetary orbital changes on Earth's atmospheric water vapor variations at time t after transformation. $F(t)$ is determined by the sum of four functions $Y_1(t)$, $Y_2(t)$, $Y_3(t)$, and $X(t)$. Functions $Y_1(t)$, $Y_2(t)$, and $Y_3(t)$ respectively represent the impact of Earth's rotation, the Moon's revolution, and Earth's revolution on Earth's atmospheric water vapor variations at time t. $X(t)$ represents the impact of the orbital changes of other planets in the solar system (excluding the Sun, Moon, and Earth) on Earth's water vapor variations at time t.

During Earth's rotation, periodic effects are produced on the diurnal variations of Earth's atmospheric water vapor. For Earth's rotation, by subtracting atmospheric water vapor data from two adjacent hours, the influence of Earth's internal variability and the orbital variations of other planets can theoretically be eliminated. Within two adjacent

hours, the overall internal changes of Earth are relatively small, and the orbital motions of the Moon's revolution, Earth's revolution, and other planetary orbits relative to Earth's rotation are also very minor. From the perspective of calculus, their impact on Earth's atmospheric water vapor can be approximately eliminated through adjacent subtraction. Furthermore, based on the analysis in Section 2.1 of the Methods, it can be seen in Figures S1, S2, and S3 that the influence of Earth's rotation on variations in atmospheric water vapor is significant. The curves of atmospheric water vapor changes over multiple consecutive days display similar daily variation trends, and the main factor affecting atmospheric water vapor variations between adjacent two hours is Earth's rotation. Therefore, we approximate the impact of Earth's rotation on the day's atmospheric water vapor by calculating the absolute value of the difference between the average atmospheric water vapor values of adjacent hours within a day (see Equation (3)). By utilizing all hourly measurements of Earth's atmospheric water vapor content within the study period (1959–2022) as the data foundation, the influence of Earth's rotation on variations in atmospheric water vapor can be quantified.

$$Y_1(t) = |E| \cos[\frac{2\pi}{\omega_1}(t_l - b_m^n)] + e \tag{3}$$

Where t_l represents the *n*-th hour of the *m*-th day in the *n*-th sidereal month. $|E|$ represents the absolute value of the difference in Earth's atmospheric water vapor between two adjacent hours; e is the exponential term, and b_m^n is an optional phase shift of $Y_1(t)$. To improve the convergence of $Y_1(t)$, it is necessary to know the number of hours of motion a priori. In the cosine term, the width ω_1 is determined by the number of hours required to complete the periodic motion.

Given the physical continuity of Earth's water vapor, we assume that the influence function of Earth's rotation on atmospheric water vapor variations (i.e., $Y_1(t)$) is continuous in all cases, including at the intersection time t_{l0} between two diurnal cycles. Here, we evaluate the continuity of the Earth's rotation function $Y_1(t)$. The $Y_1(t)$ for days m and $m+1$ can be expressed as:

$$Y_1^m(t) = |E_m| \cos[\frac{2\pi}{\omega_m}(t_l - b_m^n)] + e_m \tag{4}$$

$$Y_1^{m+1}(t) = |E_{m+1}| \cos[\frac{2\pi}{\omega_{m+1}}(t_l - b_{m+1}^n)] + e_{m+1} \tag{5}$$

To ensure that $Y_1(t)$ is continuous at the intersection time t_{l0} between two diurnal cycles, the following two constraints must be satisfied:

$$Y_1^m(t)|_{t=t_{l0}} = Y_1^{m+1}(t)|_{t=t_{l0}} \tag{6}$$

$$(\frac{\partial Y_1^m(t)}{\partial t})|_{t=t_{l0}} = (\frac{\partial Y_1^{m+1}(t)}{\partial t})|_{t=t_{l0}} \tag{7}$$

Substituting Equation (4) and Equation (5) into Equation (6) and substituting their derivatives into Equation (7) yields.

$$|E_{m+1}| = \frac{|E_m| \sin[\frac{2\pi}{\omega_m}(t_{l0} - b_m^n)]}{\sin[\frac{2\pi}{\omega_{m+1}}(t_{l0} - b_{m+1}^n)]} \tag{8}$$

$$e_{m+1} = |E_m| \cos[\frac{2\pi}{\omega_m}(t_{l0} - b_m^n)] + e_m - |E_{m+1}| \cos[\frac{2\pi}{\omega_{m+1}}(t_{l0} - b_{m+1}^n)] \quad (9)$$

From Equation (8), we can express $|E_{m+1}|$ in terms of $|E_m|$, and Equation (9) connects e_{m+1} with e_m. Similarly, substituting Equations (8) and (9) into Equation (5), we obtain the multi-day continuous model $Y_1(t)$. On day m ($m \geq 2$), the total number of free parameters in the function $Y_1(t)$ is $m+1$ (i.e., from e on the first day to b_1^n up to b_m^n). In this study, we used the Levenberg-Marquardt[40-42] minimization algorithm to estimate each free parameter and proposed a general scheme for global optimization. Except for the first day, the parameters $|E|$ and e for each subsequent day are calculated using Equations (8) and (9), respectively.

In the quantitative model of the Moon's revolution around Earth influencing variations in Earth's atmospheric water vapor, we approximately quantify the influence of the Moon's revolution by subtracting the atmospheric water vapor values of two consecutive days. From the analysis in Section 2.2 of the Methods, we know that the daily variation trend of Earth's atmospheric water vapor is mainly influenced by Earth's rotation. The similarity in daily variation trends is because Earth completes one rotation every day. Through the analysis of Figures S4 and S5, it is evident that although the daily variation trends of Earth's atmospheric water vapor are the same, the specific fluctuation values (vertical axis) of the ups and downs within a sidereal month cycle differ each day. These differences in numerical fluctuations are mainly due to the Moon's revolution around Earth affecting changes in Earth's atmospheric water vapor. Furthermore, since Earth completes its rotation cycle every day and Earth's revolution around the Sun accounts for only 1/365 of its annual orbital period in one day, the orbital changes of other planets are even smaller. Therefore, the difference between two adjacent days can approximately eliminate the influences of Earth's rotation, Earth's revolution around the Sun, other planetary orbital changes, and Earth's internal variability (see Equation (10)). To quantify the influence of the Moon's revolution on variations in Earth's atmospheric water vapor, daily atmospheric water vapor values from 1959 to 2022 were utilized as the data foundation.

$$y_n(t_s) = A_2 \cos[\frac{2\pi}{\omega_2}(t_2 - c)] + I_2 \quad (10)$$

Where A_2 represents the amplitude, c is a constant, I_2 is the exponential term, n denotes the n-th sidereal month, and t_s represents the t_s-th day of the n-th sidereal month. Theoretically, the impact of the Moon's revolution on Earth's water vapor on the t_s-th day of the n-th sidereal month in the i-th year can be expressed by $y_n(t_s)$. However, through practical analysis of atmospheric water vapor data, we found that the Moon's influence on Earth's atmospheric water vapor is irregular. Therefore, it cannot be represented by the harmonic function in Equation (10) to describe its specific period. Thus, we use Equation (11) to perform an indefinite integral calculation of the difference in atmospheric water vapor between two consecutive days to quantify the impact of the Moon's revolution around Earth on changes in Earth's atmospheric water vapor.

$$Y_2(t)_n^i = y_n(t_s) \quad (11)$$

$$Y_2(t) = \int_{t_1}^{t_2} f(t)\left|W(t+1) - W(t)\right|dt \tag{12}$$

$$f(t) = \begin{cases} a_1, & t_1 \le t < t_2 \\ a_2, & t_2 \le t < t_3 \\ \vdots & \\ a_n, & t_{n-1} \le t < t_n \end{cases} \tag{13}$$

Where $Y_2(t)$ represents the impact of the Moon's revolution on Earth's atmospheric water vapor. t_1 and t_2 are the t_1-th and t_2-th days of the n-th sidereal month, respectively. $W(t)$ represents the atmospheric water vapor content on day t. $f(t)$ is a weight function driven by atmospheric water vapor data, used to adjust the influence weights of different time periods. a represents the influence weights within each time period. In practical calculations, the function $f(t)$ is determined by analyzing and fitting historical data, and the influence weights are established based on the variations across different time periods.

Based on the analysis in Section 2.3 of the Methods, we understand that the daily variation trend of Earth's atmospheric water vapor is mainly influenced by Earth's rotation. Within one sidereal month cycle, the specific numerical fluctuations in Earth's atmospheric water vapor are primarily caused by the influence of the Moon's revolution around Earth on changes in atmospheric water vapor. Nevertheless, the numerical fluctuations of Earth's atmospheric water vapor in two adjacent sidereal months are not exactly the same and do not follow a fixed pattern, which is due to the influence of Earth's revolution on changes in Earth's atmospheric water vapor (see Figure S6). Within two consecutive months, Earth has completed 54⁄365 of its orbital revolution period around the Sun, thereby making the influence of Earth's revolution more pronounced. To quantify the influence of Earth's orbital revolution around the Sun on variations in atmospheric water vapor, we approximate the elimination of Earth's internal variability and the effects of Earth's rotation and the Moon's revolution around Earth (since they complete identical cycles) by subtracting the monthly average atmospheric water vapor values of adjacent sidereal month cycles (see Equation 14). Additionally, because the influence of other planetary orbits within a month is relatively small, subtracting the monthly averages between adjacent sidereal month cycles can also approximately eliminate the impact of other planetary orbital changes. We use the monthly average atmospheric water vapor data for all sidereal month cycles from 1959 to 2022 to quantify the impact of Earth's revolution on changes in Earth's atmospheric water vapor.

$$Y_3(t) = \left|S\right|\cos[\frac{2\pi}{\omega_3}(t-c)] + s \tag{14}$$

Where $Y_3(t)$ represents the influence of Earth's revolution on atmospheric water vapor, t denotes the hours in a year, and $\left|S\right|$ is the absolute value of the difference in monthly averages between adjacent sidereal month cycles. c and s are the exponential term and the optional phase shift, respectively. The width of ω_3 is determined by the number of hours it takes to complete its periodic motion.

To ensure that the influence function of Earth's revolution on atmospheric water vapor changes (i.e., $Y_3(t)$) is continuous in all cases, including at the intersection time t_0 between consecutive years. We evaluate the continuity of the Earth's revolution function $Y_3(t)$; $Y_3(t)$ for year *i* and year *i+1* can be expressed as:

$$Y_3^i(t) = S_i \cos[\frac{2\pi}{\omega_3^i}(t - c_i)] + s_i \tag{15}$$

$$Y_3^{i+1}(t) = |S_{i+1}| \cos[\frac{2\pi}{\omega_3^{i+1}}(t - c_{i+1})] + s_{i+1} \tag{16}$$

To ensure that $Y_3(t)$ is continuous at the junction point t_0 between two annual cycles, the following two constraints must be satisfied:

$$Y_3^i(t)\Big|_{t=t_0} = Y_3^{i+1}(t)\Big|_{t=t_0} \tag{17}$$

$$(\frac{\partial Y_3^i(t)}{\partial t})\Big|_{t=t_0} = (\frac{\partial Y_3^{i+1}(t)}{\partial t})\Big|_{t=t_0} \tag{18}$$

By substituting Equations (15) and (16) into Equation (17) and substituting its derivative into Equation (18), we obtain:

$$|S_{i+1}| = \frac{|S_i| \sin[\frac{2\pi}{\omega_3^i}(t_0 - c_i)]}{\sin[\frac{2\pi}{\omega_3^{i+1}}(t_0 - c_{i+1})]} \tag{19}$$

$$s_{i+1} = |S_i| \cos[\frac{2\pi}{\omega_3^i}(t_0 - c_i)] + s_i - |S_{i+1}| \cos[\frac{2\pi}{\omega_3^{i+1}}(t_0 - c_{i+1})] \tag{20}$$

By substituting Equations (19) and (20) into Equation (14), we obtain a continuous $Y_3(t)$ model. The total number of free parameters in the function $Y_3(t)$ for year i($i \geq 2$) is *i+1* (i.e., *s* for the first year, from c_1 to c_i). These free parameters are estimated by applying the Levenberg-Marquardt minimization algorithm. For each year, $|S|$ and s (except for the first year) are calculated using Equations (19) and (20), respectively.

$X(t)$ represents the impact of the orbital changes of other planets in the solar system (excluding the Sun, Earth, and Moon) on Earth's atmospheric water vapor variations. The influence of other planetary orbits on Earth's atmospheric water vapor changes can be determined through a physical function dependent on the planets' orbits and positions. However, establishing such a function is difficult because, although the motion of each planet can be strictly calculated, the physical mechanisms linking the motion of individual planets to Earth's atmospheric water vapor still require further research. Additionally, due to the complexity of the physical processes connecting Earth's atmospheric water vapor with the entire planetary system, we consider the combined effects of these planets together.

From the analysis in Section 2 of the Methods, we know that although Earth's atmospheric water vapor variation trend is generally similar each day throughout the year, occasionally different fluctuation patterns appear (see Figure S7). Furthermore, in the three-dimensional plot of daily variations in Earth's atmospheric water vapor from 1959 to 2022, localized irregular fluctuations can also be observed (see Figure S6D). These fluctuations are precisely caused by the influence of orbital variations of other planets on changes in Earth's atmospheric water vapor. From the analysis in Section 2.4 of the Methods, it can be seen that the periodic fluctuation phenomena of Earth's

atmospheric water vapor caused by the influences of orbital variations of different planets mainly manifest on longer interannual time scales and are irregular. Therefore, by subtracting the annual average values of Earth's atmospheric water vapor between two adjacent years, we can approximately eliminate the influence of Earth's internal variability, Earth's rotation, the Moon's revolution around Earth, and Earth's revolution around the Sun. Thus, the influence of other orbital variations is obtained, as shown in Equation.

$$X(t)=\left(\int_t^{t+1}\frac{dM(t)}{dt}dt\right)-\left(\frac{1}{n}\sum_{j=-n}^{n}\frac{\int_t^{t+1}\frac{dM(t)}{dt}dt}{\sqrt{Y_1(t)^2+Y_1(t+j)^2+\cdots+Y_3(t)^2+Y_3(t+j)^2}}\right) \quad (21)$$

Where $X(t)$ represents the impact of orbital changes of other planets on Earth's atmospheric water vapor variations. $M(t)$ is a continuous function of atmospheric water vapor values at time *t*. $\int_t^{t+1}\frac{dM(t)}{dt}dt$ denotes the change in atmospheric water vapor from year *t* to year *t+1*. $Y_1(t)$ represents the influence of Earth's rotation at time *t*, varying with time *t*. $Y_2(t)$ represents the influence of the Moon's revolution, varying with time *t*. $Y_3(t)$ represents the influence of Earth's revolution, varying with time *t*. $\frac{1}{n}\sum_{j=i-n}^{i+n}$ denotes a sliding window used to smooth out the effects of Earth's rotation, Earth's revolution, and the Moon's revolution. *n* represents the size of the time window, and *j* represents the time offset.

In this study we not only quantify the impact of different planetary orbital changes on the Earth's atmospheric water vapor changes, but also define the percentage contribution of different planetary orbital changes to the impact of Earth's atmospheric water vapor changes. This ratio is represented as the influence caused by each planet's orbital changes on Earth's atmospheric water vapor variations divided by the sum of the influences from all planetary orbital changes.

$$Z_1^i=\frac{Y_1(t)^i}{Y_1(t)^i+Y_2(t)^i+Y_3(t)^i+X(t)^i} \quad (22)$$

$$Z_2^i=\frac{Y_2(t)^i}{Y_1(t)^i+Y_2(t)^i+Y_3(t)^i+X(t)^i} \quad (23)$$

$$Z_3^i=\frac{Y_3(t)^i}{Y_1(t)^i+Y_2(t)^i+Y_3(t)^i+X(t)^i} \quad (24)$$

$$Z_X^i=\frac{X(t)^i}{Y_1(t)^i+Y_2(t)^i+Y_3(t)^i+X(t)^i} \quad (25)$$

Where Equation (22) represents the contribution of Earth's rotation to changes in Earth's atmospheric water vapor in year *i*; Equation (23) represents the contribution of the Moon's revolution to these changes in year *i*; Equation (24) represents the contribution of the Earth's revolution to the effect of water vapor changes in the Earth's atmosphere in year *i*; and Equation (25) represents the contribution of orbital changes of other planets in the solar system to these changes in year *i*.

3.2 Specific Quantification

To quantify the impact of Earth's rotation on changes in atmospheric water vapor within two consecutive hours, we employed the function $Y_1(t)$ from Equation (3) to assess the role of Earth's rotation in these variations. By utilizing the Levenberg-Marquardt algorithm, we successfully fitted a first-order derivative model to the time series of atmospheric water vapor differences between consecutive hours and solved for the unknown parameters of this function. Concurrently, using Equation (22), we calculated the average contribution of Earth's rotation to atmospheric water vapor changes during the study period. Computational analysis indicates that the average contribution of Earth's rotation to atmospheric water vapor changes during the study period is approximately 4% (see Figure 2 and Figure 3A).

Similarly, we used the function $Y_2(t)$ from Equation (12) to quantify the impact of the Moon's revolution around Earth on atmospheric water vapor changes and employed Equation (23) to calculate the average contribution of the Moon's revolution to these changes during the study period. By applying this model to calculate atmospheric water vapor changes caused by the Moon's revolution around Earth over two consecutive days, the results show that the average contribution of the Moon's revolution to atmospheric water vapor changes is approximately 10% (see Figure 2 and Figure 3B).

When quantifying the impact of Earth's revolution on atmospheric water vapor changes, we analyzed the differences in monthly average atmospheric water vapor within adjacent sidereal months. By fitting a first-order derivative model of the function $Y_3(t)$ from Equation (14) to the time series of monthly average atmospheric water vapor differences over sidereal month cycles, we obtained the unknown parameters of the relevant function. Subsequently, using Equation (24), we calculated the average contribution of Earth's revolution to atmospheric water vapor changes during the study period. The results indicate that Earth's revolution contributes approximately 71% to atmospheric water vapor changes (see Figure 2 and Figure 3C).

Furthermore, we utilized the function $X(t)$ from Equation (21) to measure the impact of orbital changes of other planets on Earth's atmospheric water vapor variations and used Equation (25) to calculate their average contribution during the study period from 1959 to 2022. In-depth analysis reveals that the average contribution of orbital changes of other planets to Earth's atmospheric water vapor variations is approximately 15% (see Figure 2 and Figure 3D).

4. Predicting future changes in water vapor in the Earth's atmosphere

LSTM (Long Short-Term Memory) is a classic deep learning model (RNN) whose uniqueness lies in its ability to predict future trend changes based on the input of the current time step and the network state output from the previous time step. This allows it to automatically learn and capture long-term dependencies and periodic patterns within long time series data[77-78]. Due to its excellent predictive capabilities, LSTM has been widely applied in various fields such as speech recognition, handwriting recognition, and time series forecasting[79-80]. The structure of LSTM consists of a chain of repeated modules that update the state through a recurrent network, effectively capturing long-term dependencies and periodicity in sequences. From the analyses in Sections 2 and 3 of the Methods, it can be seen that the orbital changes of different

planets have periodic impacts on Earth's atmospheric water vapor. Therefore, this long-term variation characteristic aligns very well with the simulation and prediction capabilities of the LSTM model.

The LSTM's recurrent unit consists of four key components: the memory cell *c*, the forget gate f_t, the input gate i_t, and the output gate O_t. These four components interact and collaborate to enable the LSTM network to better handle and retain information in sequences. The specific working principles are illustrated in Figure S10. In the second recurrent module of Figure S10, p_t is used as the input vector to the LSTM. The gates f_t, i_t, and O_t, as well as the memory cell $C_t^{'}$, are all controlled by p_t and h_{t-1}. The forget gate f_t and the input gate i_t are used to update the cell state C_t. The output gate O_t determines how much information is passed on to the next time step *t+1*. These gates are comprised of a fully connected deep learning layer with a Sigmoid activation function and an element-wise multiplication operation. The working mechanism of the gates and the flow of information can be represented as:

$$f_t = \sigma(W_f \cdot [h_{t-1}, p_t] + b_f) \tag{26}$$

$$i_t = \sigma(W_i \cdot [h_{t-1}, p_t] + b_i) \tag{27}$$

$$C^{'}_t = \tanh(W_c \cdot [h_{t-1}, p_t] + b_c) \tag{28}$$

$$C_t = f_t \odot C_{t-1} + i_t \odot C^{'}_t \tag{29}$$

$$O_t = \sigma(W_o \cdot [h_{t-1,} p_t] + b_o) \tag{30}$$

$$h_t = O_t \odot \tanh(C_t) \tag{31}$$

In this context, the transformations from the input to the gates i, f, and O are all controlled by a Sigmoid function, which $\odot$ represents element-wise multiplication. W and b denote the weights and biases, respectively. h is a hidden state, and *tanh(l)* is the hyperbolic tangent function, which performs piecewise operations on each element of the vector *l*. These equations describe the input computation, activation functions, and the flow of information within the gates of the LSTM. This structure enables the LSTM network to effectively learn and capture long-term dependencies in the input sequence.

In this study, we divided the atmospheric water vapor data from 1959 to 2022 into four-time scales: hourly, daily average, monthly average, and annual average data. Specifically, the data from 1959 to 2000 was used for model training, and the data from 2001 to 2022 was used for model testing. This data partitioning strategy ensured that the model was thoroughly tested and optimized during both the training and validation phases. In order to improve the performance of the Long Short-Term Memory (LSTM) model, we applied a Bayesian optimization method and randomly selected 10% of the data from the training dataset for the basic experiments. Extensive testing was conducted on the number of LSTM layers, ranging from 1 to 5, in combination with 1 to 3 dense layers in various configurations. The final structure was determined to be a 4-layer deep learning network with two LSTM layers and two dense layers, with neuron

counts of 64, 32, 64, and 25, respectively, in each layer. To improve training stability and convergence, batch normalization was applied to each hidden layer, and the batch size was set to 32, achieving optimal performance.

The loss function was chosen to be the Mean Square Error (MSE), which measures the deviation between the predicted and actual values of the model. After testing various gradient descent algorithms, including Adam, RMSprop, AdaGrad, Nesterov's, SGD, and Adadelta, the Adam optimizer was chosen for its superior performance across multiple tasks and datasets. Although this study utilized data on four different time scales (hourly, daily average, monthly average, and annual average), to maintain consistency and comparability of the model, all data were trained and tested using the same LSTM model parameter settings. Therefore, Figure S11 shows the best results obtained from the comprehensive evaluation of the four datasets under this model. As training epochs increased, the model's loss function gradually decreased, eventually stabilizing below 0.05, indicating that the LSTM model performed well in predicting trends in Earth's atmospheric water vapor. Additionally, Figure S11 illustrates the trends in the coefficient of determination (R^2), mean absolute error (MAE), and root mean square error (RMSE) over time steps. By analyzing these metrics, the optimal time step was determined to be 58, meaning that the model used the input sequence from the previous 58-time steps to predict the 59th time step.

Ultimately, the optimized LSTM deep learning model successfully predicted future trends in Earth's atmospheric water vapor. This trend is affected by a combination of orbital variations of the different planets and the internal variability of the Earth. The detailed results of the training and predictions are shown in Figures 4, 5, and Table 1, further verifying the model's effectiveness and accuracy.

Reference

51. Graham RM, Hudson SR, Maturilli M. Improved performance of era5 in arctic gateway relative to four global atmospheric reanalyses. *Geophysical Research Letters*, 2019, 46, 6138-6147.

52. Hersbach H, Bell B, Berrisford P, et al. The era5 global reanalysis. *Quarterly Journal of the Royal Meteorological Society*, 2020, 146, 1999-2049.

53. Yao YH, Zhang K. An Improved Self-Born Weighted Least Square Method for Cylindricity Error Evaluation. *Applied Sciences*, 2022, 12(23), 12319-12328.

54. Ahn Hyeongki, Kim Hyunchang, Choi Ahyeong, et al. Hybrid TDOA/AOA Hypocenter Localization Using the Constrained Least Squares Method with Deep Learning P-Onset Picking. *Processes*, 2022, 10(12), 2505-2516.

55. Sasayama Teruyoshi, Okamura Naoki, Higashino Kohta, et al. Improvement in magnetic nanoparticle tomography estimation accuracy by combining sLORETA and non-negative least squares methods. *Journal of Magnetism and Magnetic Materials*, 2022, 563, 169953-169960.

56. Eddy John A. The maunder minimum. *Science*, 1976, 192, 1189-1202

57. A Correspondent. Rotation of planetary atmospheres. *Nature*, 1976, 259, 16-17.

58. Scafetta N. Empirical evidence for a celestial origin of the climate oscillations and its implications. *Journal of Atmospheric and Solar-Terrestrial Physics*, 2010, 72, 951-970.

59. Piccolroaz S, Amadori M, Toffolon M. Importance of planetary rotation for ventilation processes in deep elongated lakes: Evidence from Lake Garda (Italy). *Scientific Reports*, 2019, 9, 8290-8298.

60. Westerhold T, Marwan N, Drury Anna J, et al. An astronomically dated record of earth's climate and its predictability over the last 66 million years. *Science*, 2020, 369, 1383-1387.

61. Hunt B. The effects of past variations of the Earth's rotation rate on climate. *Nature*, 1979, 281, 188–191.

62. WILLIAMS G. Effects of the Earth's rotation rate on climate. *Nature*, 1980, 286, 309–310.

63. Siscoe G. Solar–terrestrial influences on weather and climate. *Nature*, 1978, 276, 348–352.

64. Mauk FJ, Johnston M. On the triggering of volcanic eruptions by earth tides. *Journal of*

Geophysical Research, 1973, 78: 3356-3362.
65. Mauk FJ, Kienle J. Microearthquakes at st. Augustine volcano, alaska, triggered by earth tides. *Science*, 1973, 182: 386.
66. Eddy John A. The maunder minimum. *Science*, 1976, 192: 1189-1202.
67. Keeling Charles D, Whorf Timothy P. Possible forcing of global temperature by the oceanic tides. *Proceedings of the National Academy of Sciences*, 1997, 94: 8321-8328.
68. Gee H. Moonlight and global warming. *Nature*, 1999, 515, 857-859.
69. Stroup DF, Bohnenstiehl DR, Tolstoy M, et al. Pulse of the seafloor: Tidal triggering of microearthquakes at 9°50′n east pacific rise. *Geophysical Research Letters*, 2007, 34: 854-864.
70. Willson RC. Acrim3 and the total solar irradiance database. *Astrophysics and Space Science*, 2014, 352: 341-352.
71. Lin J, Qian T. Switch Between El Nino and La Nina is Caused by Subsurface Ocean Waves Likely Driven by Lunar Tidal Forcing. *Scientific Reports*, 2019, 9(1), 13106-13112.
72. Liu JY, Wu TY, Lin CY, et al. The three-dimensional plasma structures and flows of the Earth's upper atmosphere due to the Moon's gravitational force. *Scientific Reports*, 2022, 12, 21003-21010.
73. Shi XY, Chou HR, Liu YQ. VLSI Design and Implementation of Reconfigurable 46-ModeCombined-Radix-Based FFT Hardware Architecture for 3GPP-LTE Applications. *IEEETransactions on Circuits&Systems I Regular Papers*, 2017, 99, 1-12.
74. Nguyen M, To Q, Monchiet V. Derivation of FFT numerical bounds of the effective properties of composites and polycristals. *Theoretical & Applied Mechanics Letters*, 2021, 11(02), 94-101.
75. Ruckstuhl C, Philipona R, Morland J, et al. Observed relationship between surface specific humidity, integrated water vapor, and longwave downward radiation at different altitudes. *Journal of Geophysical Research Atmospheres*, 2007, 112, 3302-3309.
76. O'Gorman P.A, Sensitivity of tropical precipitation extremes to climate change. *Nature Geoscience*, 2012, 5: 697-700.
77. Markowsky G. A retelling of Newton's work on Kepler's Laws. *Expositions Mathematicae*, 2011, 29(3): 253-282.
78. Xiao C, Chen N, Hu C, et al. Short and mid-term sea surface temperature prediction using time-series satellite data and lstm-adaboost combination approach. *Remote Sensing of Environment*, 2019, 233: 111358-111369.
79. Fan ST, Xiao NH, Dong S. A novel model to predict significant wave height based on long short-term memory network. *Ocean Engineering*, 2020, 205, 0029-8018.
80. Karevan Z, Suykens J. Transductive LSTM for time-series prediction: An application to weather forecasting. *Neural Networks*, 2020, 125, 1-9.

Author contributions: KM designed the research. LX and KM developed the methodology. LX, KM, Bateni and MC contributed to the results analysis and discussion and drafted the manuscript. LX, KM, Bateni, MC, TD, ZD, BA, ZY and MM revised the manuscript.

Competing interests: The authors declare no competing financial interests.

Data availability statement: The data that support the findings of this study are openly available in the Open Science Framework data repository.

Acknowledgments: The authors thank the U.S. Department of Energy's Office of Science Biological and Environmental Research (BER), the National Oceanic and Atmospheric Administration (NOAA) Office of Climate Programs, the NOAA Physical Sciences Laboratory, and the European Centre for Medium-Range Weather Forecasts (ECMWF) for providing climate reanalysis data, the Scripps Institution of Oceanography for providing carbon dioxide concentrations, and the NASA Jet Propulsion Laboratory Development Ephemeris for the solar system ephemeris, and the International Earth Rotation and Reference Systems Service Rapid Service/Prediction

Centre for daylength data.

Funding: Key Project of Natural Science Foundation of Ningxia Department of Science and Technology (No. 2024AC02032), Fengyun Satellite Application Pilot Program "Development and Application of Fengyun all-weather Land Surface Temperature Spatiotemporal Fusion Dataset" (FY-APP-2022.0205).

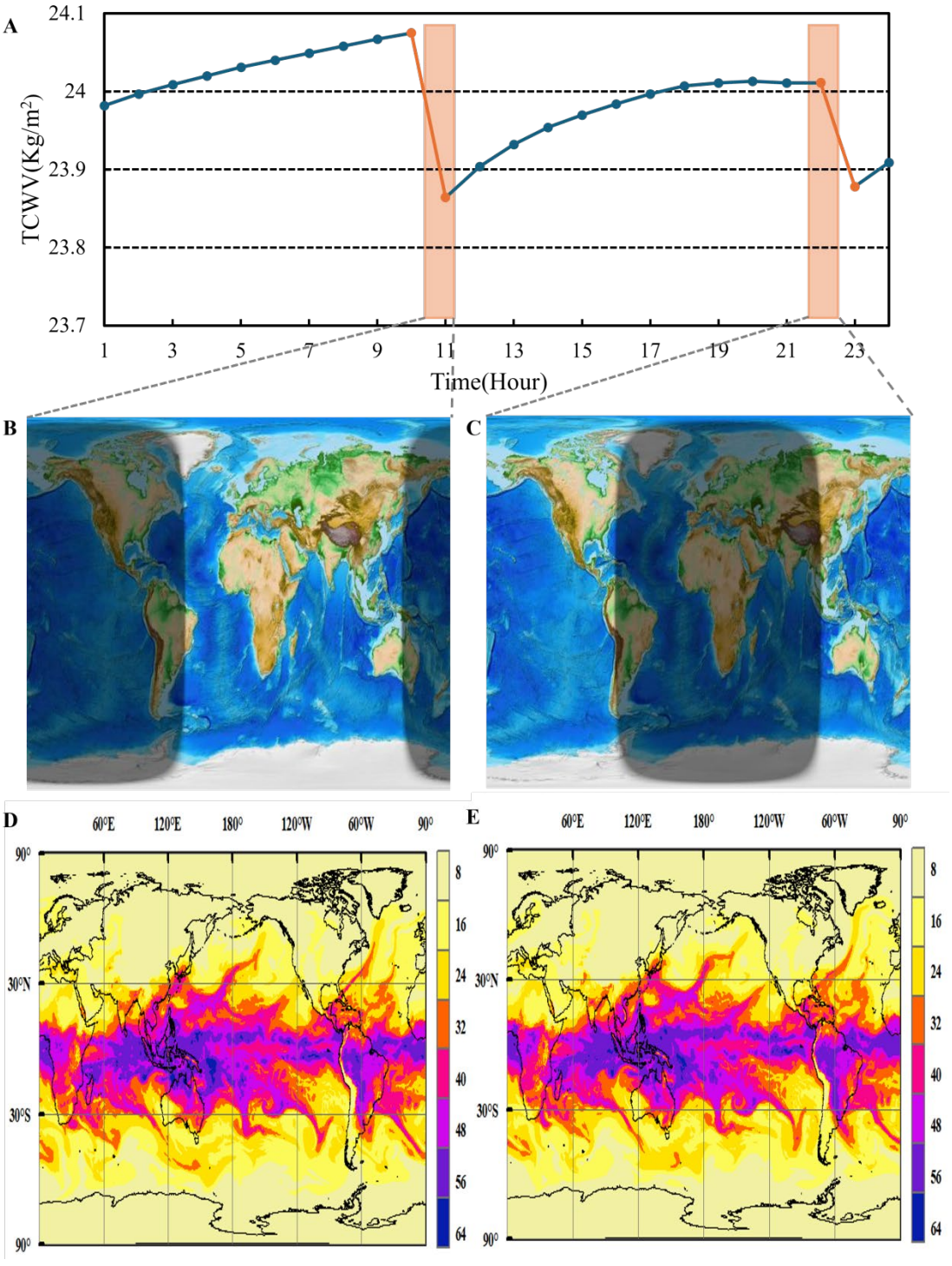

Figure S1. (A) Hourly variations in Earth's atmospheric water vapor on the 2021 vernal equinox. (B) and (C) Land and sea distribution of sunlight at UTC 11:00 and UTC 23:00 on the 2021 vernal equinox. (D) and (E) Spatial distribution of Earth's atmospheric water vapor at UTC 11:00 and UTC 23:00 on the 2021 vernal equinox.

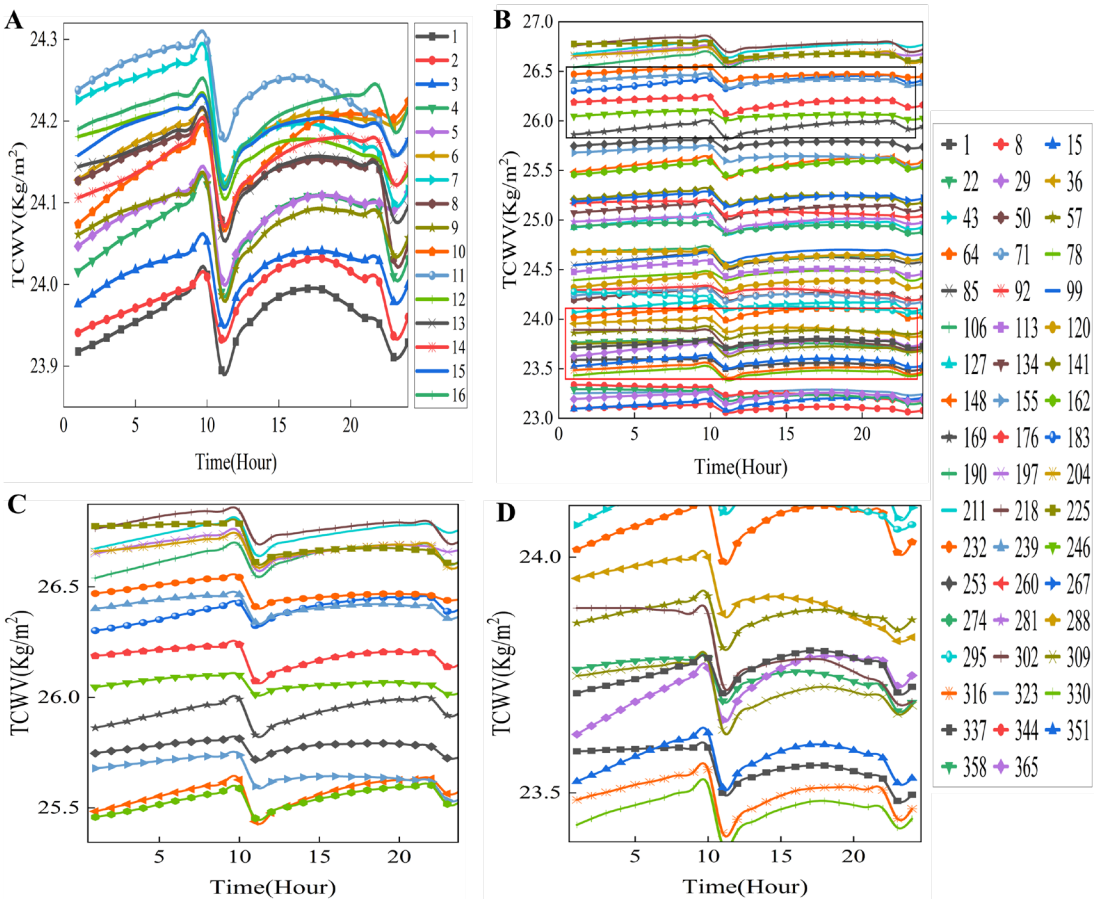

Figure S2. Hourly variations in Earth's atmospheric water vapor in 2017, with numbers in the legend representing the corresponding days. (A) Hourly variations in Earth's atmospheric water vapor from January 1 to January 16, 2017. (B) Hourly variations in Earth's atmospheric water vapor every 8 days throughout 2017. (C) Localized enlarged view of the black region in Figure S2B. (D) Localized enlarged view of the red region in Figure S2B.

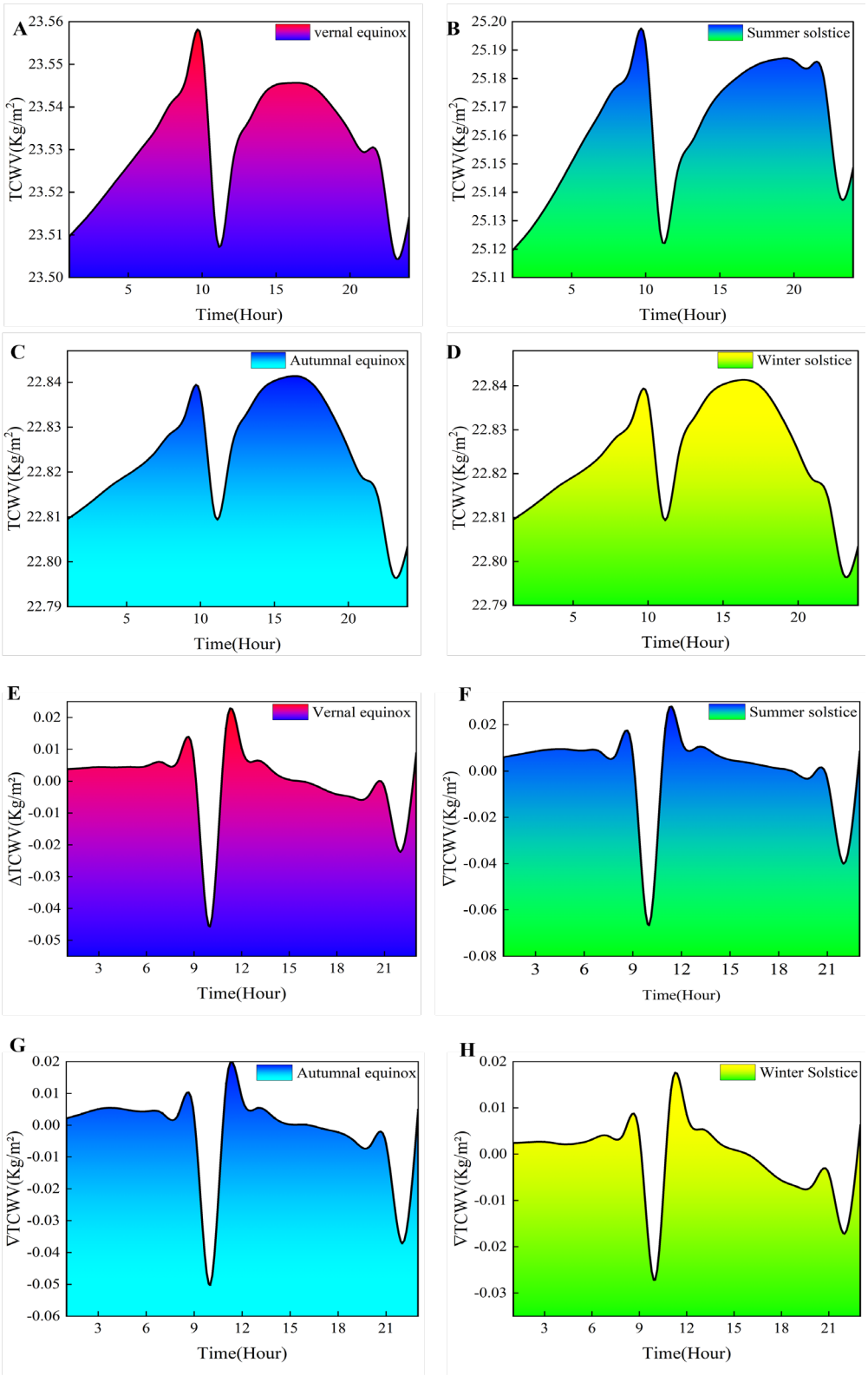

Figure S3. Daily average variations in Earth's atmospheric water vapor for different seasons from 1959 to 2022. (A) Daily average variations in Earth's atmospheric water vapor on the vernal equinox for all years. (B) Daily average variations in Earth's atmospheric water vapor on the summer solstice for all years. (C) Daily average variations in Earth's atmospheric water vapor on the autumnal equinox for all years. (D) Daily average variations in Earth's atmospheric water vapor on the winter solstice for all years. (E) Average atmospheric water vapor difference between two adjacent UTC

times on the vernal equinox for all years. (F) Average atmospheric water vapor difference between two adjacent UTC times on the summer solstice for all years. (G) Average atmospheric water vapor difference between two adjacent UTC times on the autumnal equinox for all years. (H) Average atmospheric water vapor difference between two adjacent UTC times on the winter solstice for all years.

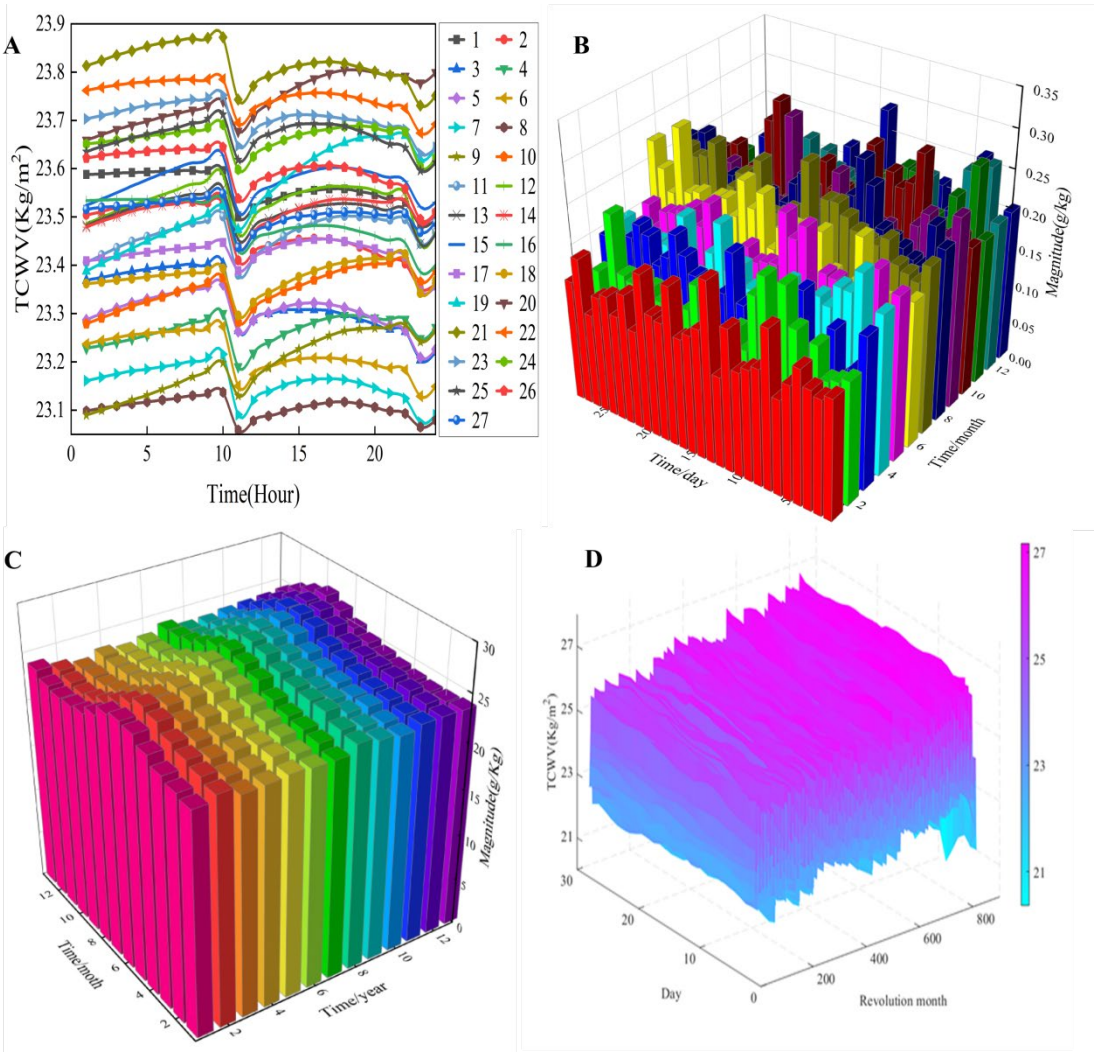

Figure S4. (A) Daily variations in Earth's atmospheric water vapor during the first sidereal month cycle of 2017. (B) Daily average variations in Earth's atmospheric water vapor across 13 sidereal month cycles in 2017. (C) Monthly average variations in Earth's atmospheric water vapor during the sidereal month cycles from 1979 to 1992. (D) Daily average variations in Earth's atmospheric water vapor across 856 global sidereal month cycles from 1959 to 2022.

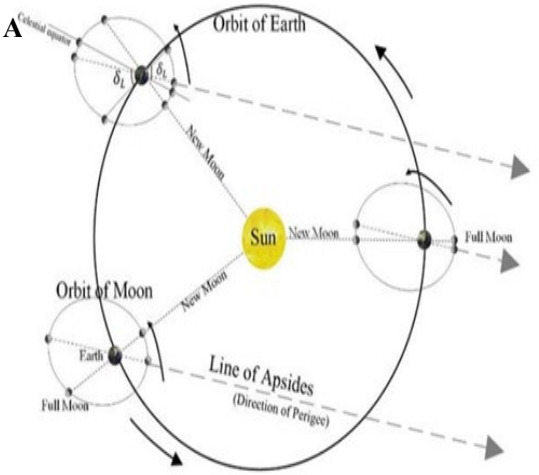
A
Orbit of Earth
Sun
New Moon
Full Moon
Orbit of Moon
Earth
Line of Apsides
(Direction of Perigee)

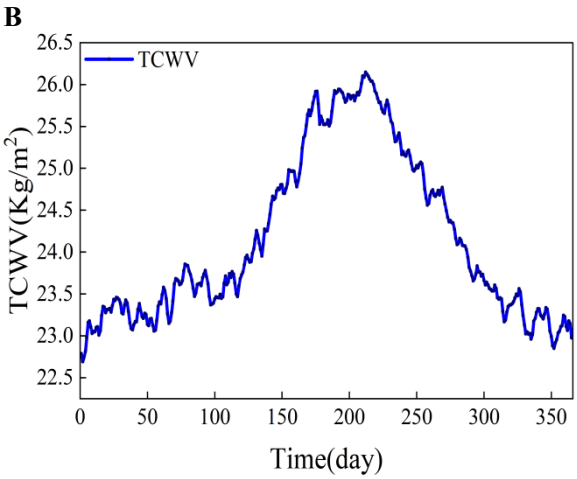
B
TCWV
TCWV(Kg/m²)
Time(day)

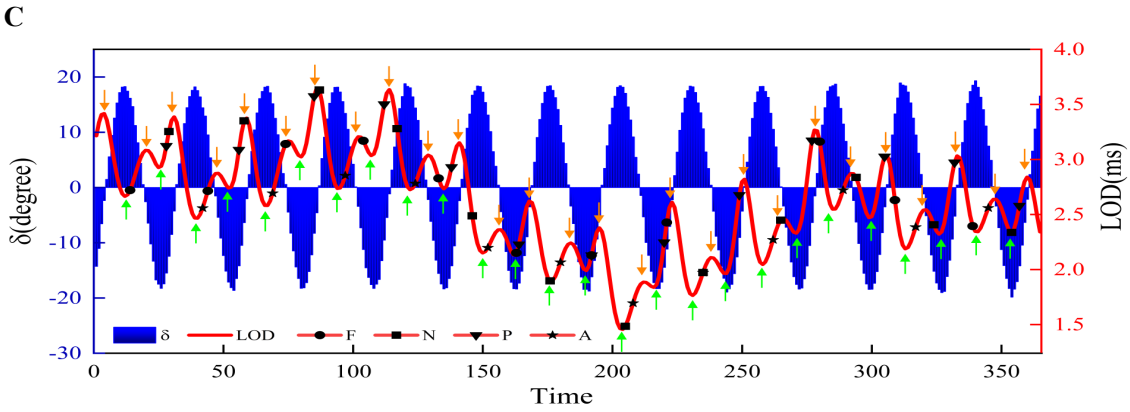
C
δ(degree)
LOD(ms)
δ
LOD
F
N
P
A
Time

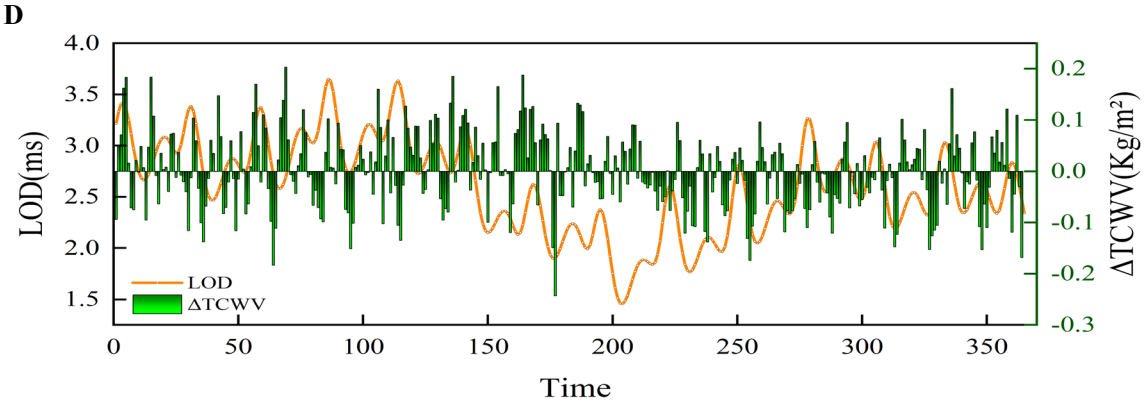
D
LOD(ms)
ΔTCWV(Kg/m²)
LOD
ΔTCWV
Time

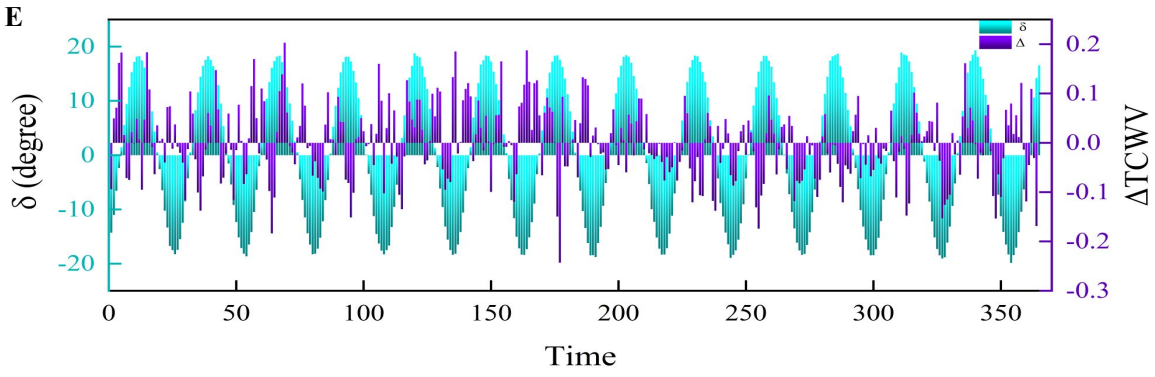
E
δ (degree)
ΔTCWV
Time

Figure S5. (A) Schematic diagram of the Moon orbiting Earth on an inclined orbit relative to the celestial equator. This schematic also depicts that during the Moon's revolution around Earth, the Moon's declination angle, lunar phase, and the distance between the Moon and Earth undergo periodic changes. (B) Changes in the daily average atmospheric water vapor of Earth in 1979. (C) Time variations of the Moon's declination angle, the distance between the Moon and Earth, and the Length of Day (LOD) over two consecutive days from January 1, 1979, to December 31, 1979. (D) Time variations of water vapor differences and LOD over two consecutive days from January 1, 1979, to December 31, 1979. (E) Time variations of water vapor differences and the Moon's declination angle over two consecutive days from January 1, 1979, to December 31, 1979. The orange and green arrows respectively represent days when the Moon's declination angle(δ) is at its maximum and zero (i.e., when the Moon is on the celestial equator).

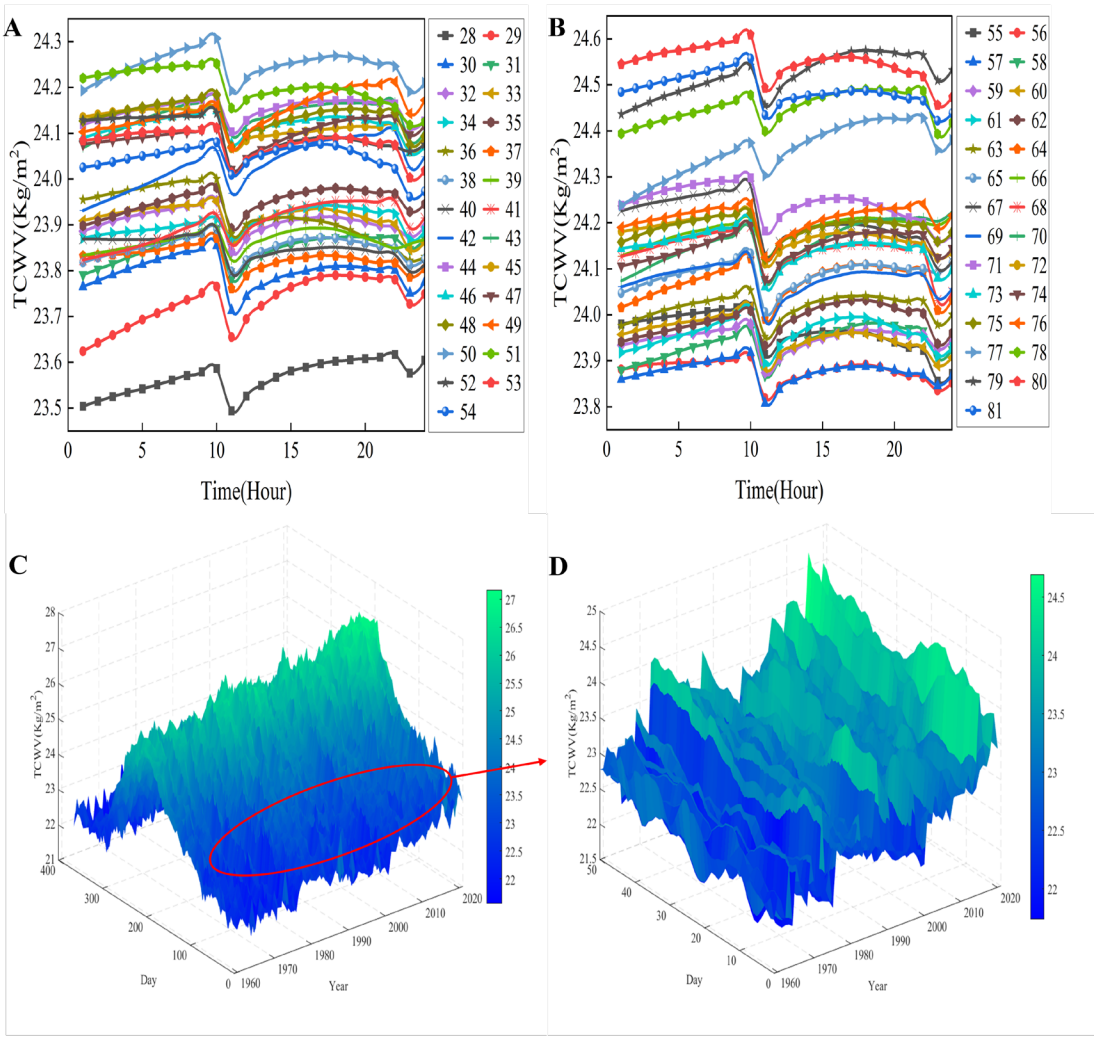

Figure S6. (A) Daily variations in Earth's atmospheric water vapor during the second sidereal month cycle in 2017. (B) Daily variations in Earth's atmospheric water vapor during the third sidereal month cycle in 2017. (C) Fluctuations in the daily average atmospheric water vapor of Earth during Earth's revolution cycles from 1959 to 2022. (D) Local detailed fluctuations in Earth's atmospheric water vapor over 50 days within Earth's revolution cycles from 1959 to 2022.

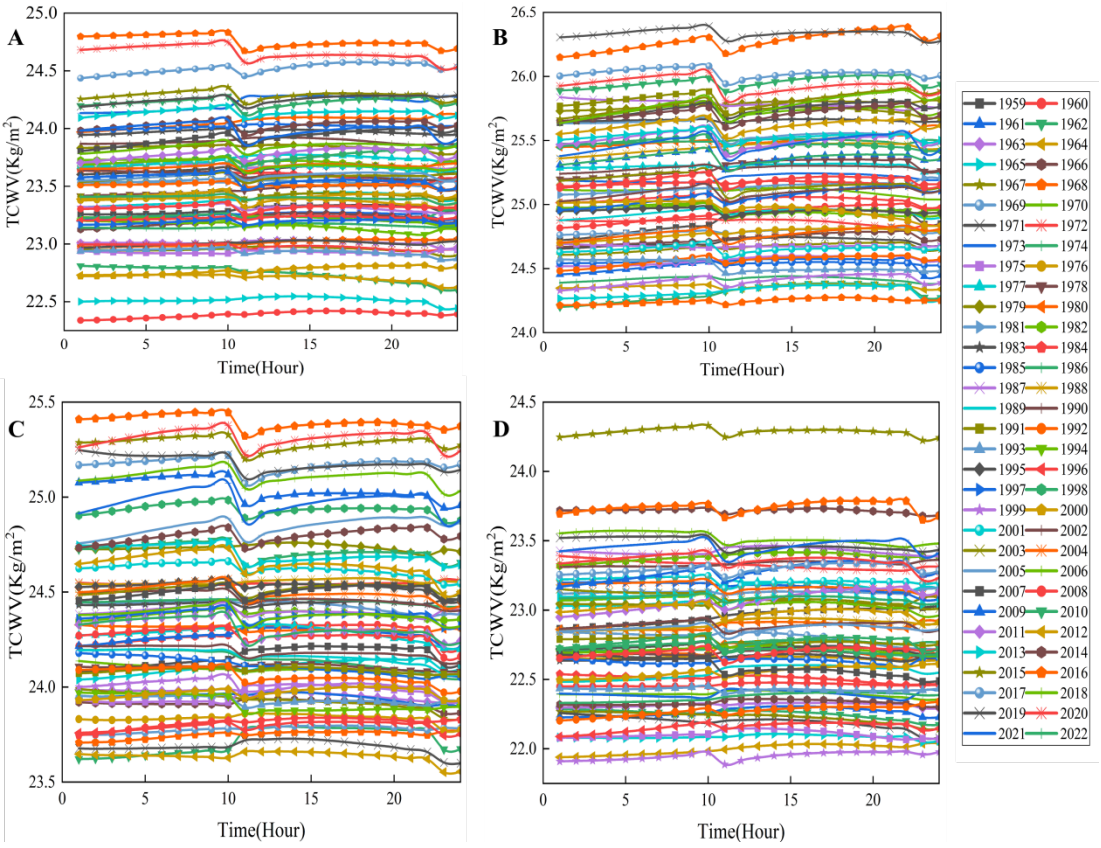

Figure S7. Variations in Earth's atmospheric water vapor for different years and seasons from 1959 to 2022. (A) Changes in Earth's atmospheric water vapor on the vernal equinox each year. (B) Changes in Earth's atmospheric water vapor on the summer solstice each year. (C) Changes in Earth's atmospheric water vapor on the autumnal equinox each year. (D) Changes in Earth's atmospheric water vapor on the winter solstice each year.

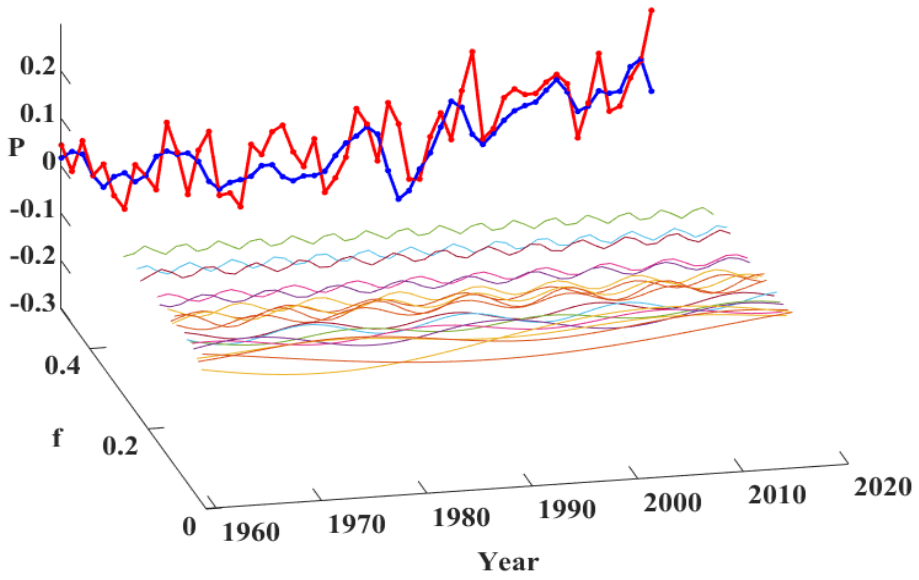

Figure S8. Reconstruction of the effects of planetary orbital changes on water vapor changes in the Earth's atmosphere based on FFT analysis methods.

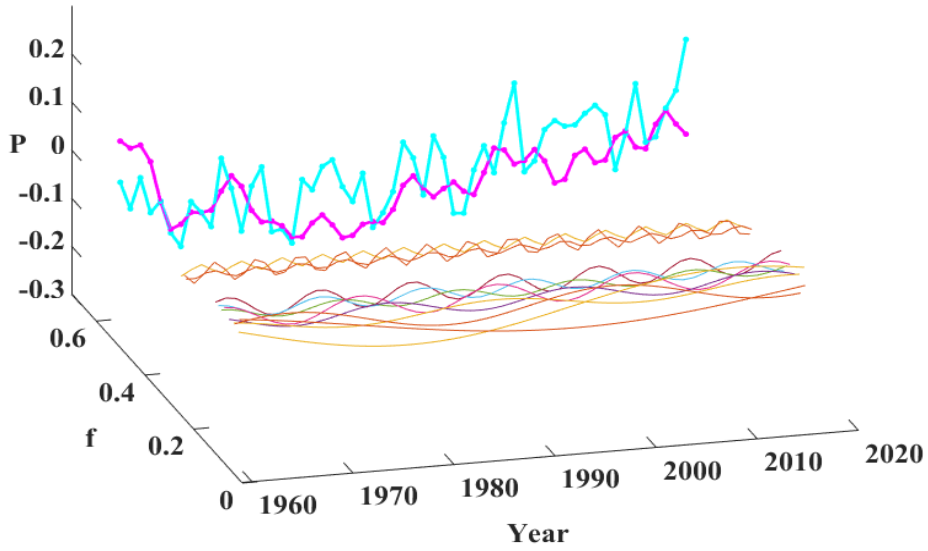

Figure S9. Reconstruction of the impact of planetary orbital changes on Earth's atmospheric water vapor variations using the MTM analysis method.

Table S1. Comparison of Planetary Orbital Periods Captured by FFT Analysis Method with Actual Orbital Periods

TCWV Period (years)	Planetary Orbital Period (years)	Specific Meaning of Orbital Period
3.5、4.1	4	Proposed four-year tidal cycle
8.25、8.5、8.9	8.9-9.4	Solar sunspot cycle
9.15	~9.1	Long-term lunar cycle
9.85	~10	Jupiter and Saturn's Ascension-Solstice Cycle
13.4	9.9-13.035	Solar sunspot cycle
15.05、18.28	18.61	Moon-Sun node cycle
21.3	19.858、19.99	Solstice cycle of Jupiter and Saturn (19.858 years) Similar solstice period for Mercury (19.99 years)
32	~30	Saturn's cycle（29.42years） Earth's pole shift cycle (29.8 years) Saturn-like solstice cycle (30.02 years)
61	~60	Repetition of Jupiter and Saturn's joint orbit (~60 years)

Table S2. Comparison of Planetary Orbital Periods Captured by MTM Analysis Method with Actual Orbital Periods

TCWV Period (years)	Planetary Orbital Period (years)	Specific Meaning of Orbital Period
4、4.1	4	Proposed four-year tidal cycle
9.15	~9.1	Long-term lunar cycle
13.4	9.9-13.035	Solar sunspot cycle
18.28	18.61	Moon-Sun node cycle
28.4	29.42	Saturn's cycle (29.42 years)
32	~30	Earth's polar shift cycle (29.8 years) Saturn's similar solstice cycle (30.02 years)
61	~60	Repetition of Jupiter and Saturn's joint orbit (~60 years)

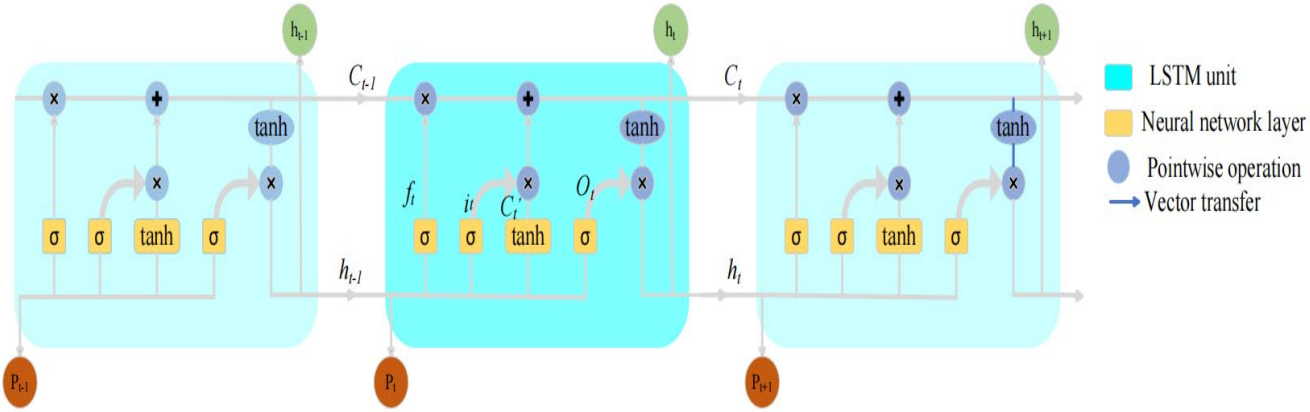

Figure S10. schematic diagram of LSTM neural network.

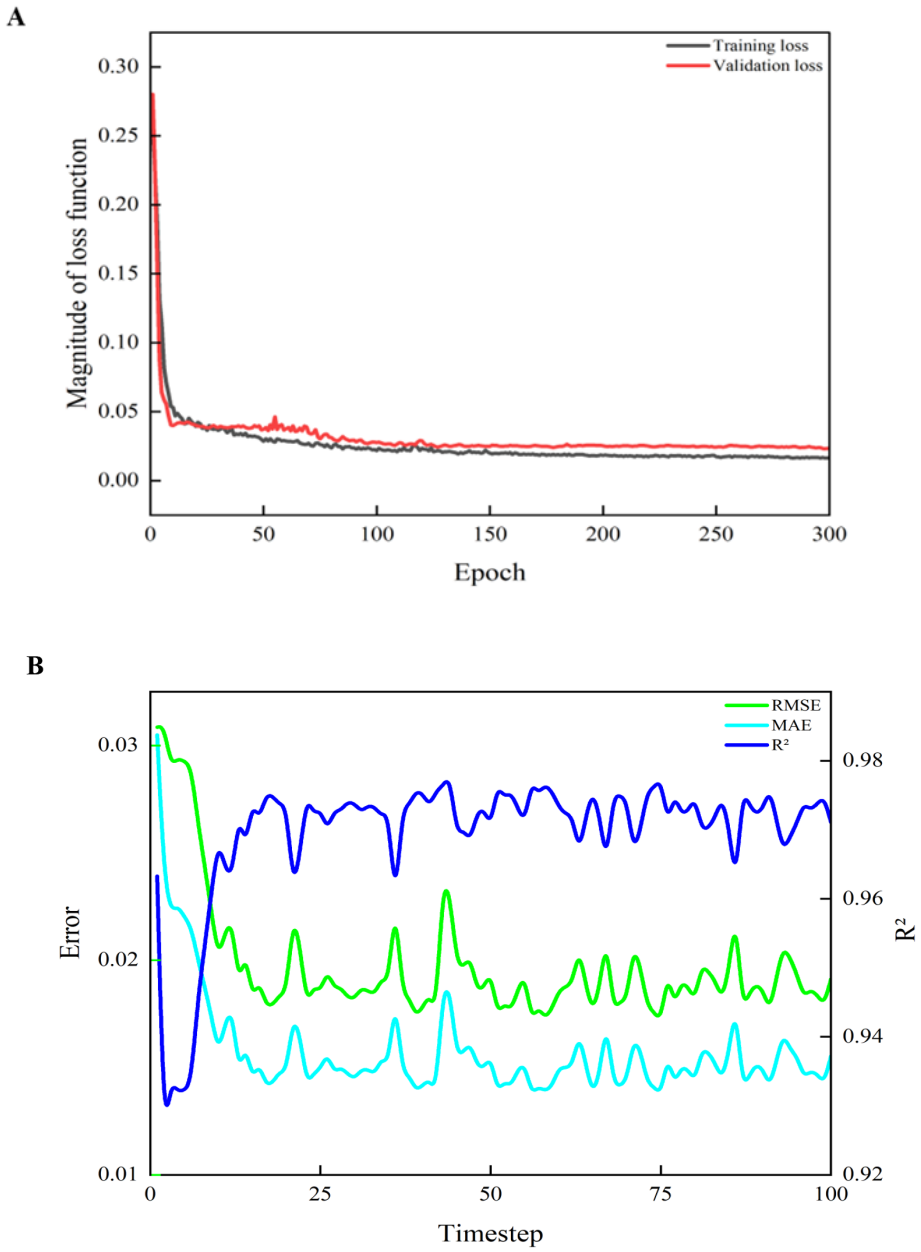

Figure S11. (A) Changes in the loss function of the network's training and testing sets over time. (B) Relationship between LSTM accuracy and time steps.